Title
Adaptive Survival Capsules for Developing Shark Embryos

Author
Goh, Rubayn

Publication Date
2021

UNIVERSITY OF CALIFORNIA

Santa Barbara

Adaptive Survival Capsules for Developing Shark Embryos

A dissertation submitted in partial satisfaction of the
requirements for the degree Doctor of Philosophy
in Materials

by

Rubayn Goh

Committee in charge:
Professor J. Herbert Waite, Co-chair
Professor Rachel A. Segalman, Co-chair
Professor Omar A. Saleh
Professor Megan T. Valentine

September 2021

The dissertation of Rubayn Goh is approved.

Omar A. Saleh

Megan T. Valentine

Rachel A. Segalman, Committee Co-chair

J. Herbert Waite, Committee Co-chair

July 2021

Adaptive Survival Capsules for Developing Shark Embryos

by

Rubayn Goh

This thesis is dedicated to my ever-supportive parents, my beautiful wife, and my son.

Desmond Goh
Eileen Tay
Janice Law
Dylan Goh

To my incredible parents, thank you for always being there for me and providing me with the proverbial 'cushion' for whenever I fall, allowing me to pursue dreams which might not always be the most pragmatic.

To my loving wife, bumping into you was perhaps the most serendipitous blessing I could have asked for. I cannot express how grateful I am for your support during the most difficult times of my Ph.D., and for always being the one pushing me forward when I am at my lowest.

To my bright-eyed son, although I would always regret missing out on the past eight months, I will be looking forward to watching you become the amazing person you are meant to be. Stay inquisitive and keep on learning.

Acknowledgements

“A lot of the things that have been accomplished in science have been accomplished on the basis of ignorance. Because once you have an established science, it has got its high priests — the guys who know everything that will work or won't work. And they don't want to be bothered. So you have to have a challenge. And the great thing is that young people are ignorant, and we should catch them before they turn into the priesthood. So I think science should have a much more daring approach.”

— Dr Sydney Brenner

I would like to thank Herb, who was more than just a PI, for his confidence, trust, and his patience throughout my Ph.D. He was never one to shy away from a problem ‘too difficult’ to solve. Herb’s unwavering dedication to basic research and pursuit of a fundamental understanding of noteworthy biological materials had been a great inspiration and motivation throughout my Ph.D. I will miss the conversations we had, his witty responses, and his often-cryptic wordplays that would, more often than not, have me scratching my head.

Secondly, I would like to thank my co-advisor, Rachel, for being supportive of my decisions and providing me the space and opportunity for learning during my formative Ph.D. years. Despite eventually veering off to pursue my interest in biological materials, I would always carry the soft skills she has taught during my first 3 years — the ‘x-axis’ being one of the many.

Finally, I would like to thank all my collaborators, mentors, friends, and family who have helped me throughout my Ph.D., either with technical expertise, hosting me while I was in Singapore, or by being a pillar of support for the past 6 years.

Vita of Rubayn Goh
September 2021

Education

PhD in Materials 2021
University of California, Santa Barbara, USA

B.Eng. in Materials Science and Engineering 2014
Nanyang Technological University, Singapore

Diploma in Biotechnology (Specialized in Veterinary Science) 2009
Temasek Polytechnic, Singapore

Awards

National Science Scholarship 2015 — 2020
Agency for Science, Technology and Research

Materials Science and Engineering Class of 2014, Valedictorian 2014
Nanyang Technological University

A*STAR Undergraduate Scholarship 2012 — 2014
Agency for Science, Technology and Research

Oral and Poster Presentation

Goh, R., “Adaptive Survival Capsules for Developing Shark Embryos”, *Invited Speaker*, Materials Research Outreach Symposium, University of California, Santa Barbara (2020).

Goh, R., J.H. Waite, “Structure-mechanics correlation of multi-functional swell shark egg cases”, The 8th International Conference on Mechanics of Biomaterials and Tissues, Waikoloa Beach, HI (2019).

Publications

1. **R. Goh**, S. Danielsen, E. Schaible, R. McMeeking, J. H. Waite, Nanolatticed architecture mitigates damage in shark eggcases. *Submitted* (2021).

2. **R. Goh**, E. Yoshida, E. Schaible, R. Behrens, C. Monnier, B. Killingsworth, K. W. Kong, S. H. Hiew, A. Miserez, S. Hoon, J. H. Waite, Nanolattice-forming hybrid collagens in protective shark eggcases. *In prep* (2021).

3. H. Papananou, R. Katsumata, Z. Neary, **R. Goh**, R. Limary, R. Segalman, Dopamine mediated polymer coating facilitates area selective Atomic Layer Deposition. *Submitted* (2021).

4. A. Kumar, H. Mohanram, K. W. Kong, **R. Goh**, S. Hoon, J. Lescar, A. Miserez, Supramolecular propensity of suckerin proteins is driven by β-sheets and aromatic interactions as revealed by solution NMR. *Biomater. Sci.* **6**, 2440–2447 (2018).

5. A. M. Brzozowska, S. Maassen, **R. Goh Zhi Rong**, P. I. Benke, C.-S. Lim, E. M. Marzinelli, D. Jańczewski, S. L.-M. Teo, G. J. Vancso, Effect of Variations in Micropatterns and Surface Modulus on Marine Fouling of Engineering Polymers. *ACS Appl. Mater. Interfaces*. **9**, 17508–17516 (2017).

6. Y.-Q. Li, B. Zhu, Y. Li, W. R. Leow, **R. Goh**, B. Ma, E. Fong, M. Tang, X. Chen, A Synergistic Capture Strategy for Enhanced Detection and Elimination of Bacteria. *Angewandte Chemie*. **126**, 5947–5951 (2014).

List of Abbreviations

BCT	Body-centered tetragonal
DTT	Dithiothreitol
gC1q	C1q globular domain
LC	Liquid crystalline
LC	Liquid crystalline elastomer
LC-MS/MS	Liquid chromatography with tandem mass spectrometry
NC	Non-collagenous
PAS	Periodic acid-Schiff
SAXS	Small angle X-ray scattering
SCR	Short consensus repeat
TEM	Transmission electron microscopy
W_f	Work to failure
ε	Strain

ABSTRACT

Adaptive Survival Capsules for Developing Shark Embryos

by

Rubayn Goh

The eggcase of swell sharks ranks among the toughest permeable membranes known. It possesses an intricate, hierarchically ordered structure that is designed to protect delicate embryos from the external environment while enabling respiratory and metabolic exchange, achieving a tactical balance between conflicting properties — porosity and toughness.

A central concept that is not well understood is how its structural adaptations play a role in its mechanical properties. Structural analyses revealed three distinct hierarchical architectural adaptations to enhance eggcase survival: Bouligand-like organization, a non-cylindrical fibril geometry, and a nanolattice architecture. Using electron microscopy and *in-situ* small angle X-ray scattering during mechanical testing, we elucidated a stepwise cumulative deformation mechanism in the eggcase with indications of lattice-governed deformation mechanisms.

Key to the distinctive and enabling nanoarchitecture is a pH-driven assembly process of liquid crystalline collagenous proteins. However, the enabling molecular structure of the eggcase-forming proteins has long eluded identification due to its highly crosslinked nature and consequent insolubility. By leveraging RNA-sequencing and proteomic techniques, we discovered a new cohort of proteins, purseins, in the swell shark gland transcriptome. Characteristic of purseins is a series of contiguous domains comprising a collagenous midblock flanked by domains typically associated with the complement of innate immunity and network-forming collagens, type VIII and X. Structurally homologous proteins were also identified in the genome of other egg-producing cartilaginous fishes, suggesting a conserved molecular strategy across species including the whale shark and the elephant shark.

CONTENTS

1 INTRODUCTION

The advancement of civilizations throughout history depended on significant improvements in materials processing, resulting in well demarcated periods of stone, bronze, and iron usage. However, less-known are the exploitations of biological materials. Owing to its elasticity, animal sinew has been used for sutures, bows, and impressively, for torsion siege engines during warfare[1]. In addition, the significant contribution of fibrous plants, keratinous wools, and silk proteins that have been used in linen, wool, and silk textile manufacture. This played an enormous role in insulating humans from the environment. Even in modern times, humanity's innovative use of biological materials plays a significant yet understated role in our daily activities — structural wooden supports, cellulose paper, plant dyes, and horseshoe crab blood[2] being a few. The advent of plastics in the 20th century lifted the constraints of reliance on natural materials and, along with sophisticated techniques, plastics can be shaped to comply with any requirements of human whim. Consequently, bio-inspired material innovations that leverage the processability of plastics such as Velcro — inspired from the burrs of the cocklebur plant — came along[3].

Advancements of characterization tools and techniques in the recent century made the investigation of microstructure, nanostructure, and all the way down to the molecular structure possible. Improvements in what can now be observed resulted in innovative bio-inspired strategies. For example, antifouling and drag reduction strategies inspired from the dermal riblet on shark skin[4,5], tough ceramics from abalone shells[6], and underwater adhesives from mussel adhesive plaques[7,8]. Besides underwater adhesives, understanding the biochemical toolbox that mussels deploy to survive the turbulent intertidal zone has also given rise to novel strategies for toughening elastomers and self-healing gels as well[9,10]. These ideas that spur pioneering solutions are grounded in the discovery and understanding of the relationships between function and biochemical structures in nature.

1.1 PROTECTIVE STRUCTURES OF DELICATE EMBRYOS AND THE EGGCASES OF SWELL SHARKS

Protective structures of delicate embryos play a decisive role in the life-and-death of a species. Through selection pressure, species have evolved unique eggcases best adapted for surviving the unique challenges of their natural habitat. The archetypal calcareous avian egg represents just one of the many kinds of protective structure for delicate embryos. Despite being rigid, the brittle calcareous eggshell would not survive the turbulent environment that whelks live and lay their eggs. Vice versa, whelk eggcases would dehydrate in the air, leading to the demise of the larvae. Recent cutting-edge research on the protein structure of these eggcases has elucidated novel molecular toughening strategies.

Even within marine animals, the strategies elucidated are fascinatingly diverse. The elastomeric eggcase of the channeled whelk undergoes a solid-state phase transition — a mechanism remarkably similar to the phase transformation toughening seen in zirconia.

The energy-dissipative solid-state phase transition of the whelk eggcase involves an α-helix coiled coil to β-sheet transition, that is non-entropic, unlike rubber[11]. These coiled-coil structures are also seen in keratins of hair, nail and scale and the praying mantis ootheca[11–14]. On the other hand, cuttlefish eggs are encapsulated in glycosylated cysteine-rich proteins with bacteriostatic properties[15]. Cysteine-rich proteins are also found in various avian, reptile, and insect eggs[16,17].

Typically seen in museums, eggcases of cartilaginous fishes (chondrichthyans), colloquially known as 'mermaid's purses', have long been an object of fascination. The *Chondrichthyes* class can be subdivided into *Elasmobranchii* (sharks, rays, skates and sawfish) and *Holocephali* (chimaeras). Earlier reports on elasmobranch eggcases misclassified them as keratinous owing to their high sulfur contents. It was only till later when investigations into the X-ray diffraction patterns elucidated the presence of collagenous triple helices[18,19]. Microscopic ultrastructural scrutiny revealed a fascinating lattice architecture[19]. This unique architecture accommodates the required permeability for respiratory and metabolic waste exchange[20] and mechanical toughness. Mechanical toughness necessary for the physical protection of the embryos, and porosities that are necessary for permeability, are contradicting traits. The elasmobranchs have accomplished both in the fabrication of the protective eggcase and therefore, would serve as an excellent model system for developing an understanding behind the design principles of a tough yet permeable membrane.

Swell sharks, *Cephaloscyllium ventriosum*, are oviparous (egg-laying) elasmobranchs endemic to the coast of Central California. The goal of this dissertation is to elucidate the mechanical, structural, and biochemical properties of the swell shark eggcase. A more in-depth discussion on the background of elasmobranch eggcases will be covered in the subsequent sub-chapters.

1.2 ULTRASTRUCTURE OF ELASMOBRANCH EGGCASES

Chondrichthyan eggcases are thick-walled rubbery structures that come in various forms. Regardless of these variations, the eggcase serves as a protective pouch-like structure that encapsulates the developing embryo for the entirety of its development till it hatches as a juvenile. Depending on the species, this can last from several months to years[21]. While most shark and skate eggcases look similar and have tendrils extending from each corner for anchoring to kelp and structures, the eggcases of *Heterodontus spp.* are auger-shaped and are typically found wedged into crevices for protection against predators[22,23]. On the other hand, the eggcases of chimaeras that are laid on the bottom of the seafloor resemble spindles with lateral fins [21].

Investigation into the ultrastructure of the lesser-spotted dogfish, *Scyliorhinus canicula,* eggcase revealed an intricate and hierarchically ordered structure that spans multiple length scales. The eggcases are comprised of a collagenous mid-layer along with an inner and outer cuticle. The cuticles are ~20% of the total thickness of the dogfish eggcase (~300 µm). The cuticles occupy a smaller volume fraction in the swell shark eggcase owing to its thicker collagenous mid-layer. The outer cuticle of the dogfish eggcase, L1, is approximately 25 µm thick and contains tyrosine-rich, oxidatively crosslinked, hydrophobic granules that are ~2 µm in diameter, and surrounded by collagenous fibrils. The crosslinking process is proposed to involve DOPA, peroxidase, and catechol oxidase[24]. The inner cuticle can be further distinguished into two layers, L3 and L4. L3 appears to be collagenous like L1 but appears to be more homogenous. L4 is thought to be comprised mainly of glycosaminoglycan[25]. Similar structures were observed in the eggcases of species belonging to the genera of *Galeus*[26], *Raja*, *Scyliorhinus*, and *Chiloscyllium* as well[27].

The mid-layer, L2, constitutes the bulk of the eggcase. This layer is composed of a collagenous architecture assembled into multiple length scales of hierarchy. At the highest length scale, the eggcase was seen to be made of laminates. Further investigation into the ultrastructure of the dogfish eggcase, revealed uniaxially oriented fibers within each layer with an ~45˚ rotation from layer to layer resulting in a Bouligand-like twist. This rotation angle seems to vary from species to species. The eggcase of *Raja spp.* is said to have fibers that are oriented approximately perpendicular from one layer to another[28].

Analyses with small angle X-ray scattering (SAXS) revealed diffraction peaks corresponding to a *d*-spacing of ~40 nm arising from the alternate banding of high and low electron densities. Observations with transmission electron microscopy (TEM) elucidated the underlying nanolattice architecture that forms these fibrils which gives rise to the diffraction peak seen with SAXS. The primary diffraction originates from the double banded structure perpendicular to the long axis of the tetragonal nanolattice. This results in a diffraction pattern similar to a lamellar phase where $q/q^* = 1, 2, 3...$, which is also observed in the auger-shaped eggcase of the Port Jackson shark[29]. In the dogfish eggcase, these diffraction peaks appear pseudo-isotropic due to the Bouligand-like twists seen in the hierarchical arrangement of these fibers. On the other hand, the diffraction peaks arising from the vane material of the Port Jackson shark eggcase showed a single orientation, indicating an uniaxial arrangement of the fibers along the vanes. A space group symmetry of I422 was assigned to the nanolattice structure based on TEM observations along the three principal axes of the unit cell[30]. Comprehensive analysis of the dogfish eggcase on the diffraction pattern from along orthogonal axes provided additional evidence of I422 symmetry with lattice parameters of $a = b = 11.6$ nm, $c = 81.6$ nm[31]. The absence of the (hk0) reflections during through-plane transmission SAXS was attributed to obscuring of features caused by overlaying of more intense features arising from multiple orientations[29,31]. Speculative models involving kinked molecular fibrils to rationalize the origins of these structures were subsequently developed by Knight and Hunt[32], and built on by Gathercole et al.[29], and Knupp et al.[30,33]. The most recent model developed by Knupp et al.[33] brings together consideration of the unit cell symmetry, high-resolution TEM observations of metal shadowed, deep-etched replicas of the dogfish eggcase, and dimensions of the single molecule building block[22]. The proposed molecular arrangement within the unit cell involves an octameric heat-to-tail arrangement of staggered fibrillar molecules. The arrangement comprises four ~45 nm kinked molecules with globular end domains that are anti-parallel and staggered by 13 nm with respect to the other four molecules of the octamer[33].

As emphasized by the fibrillar molecular structure and the intermolecular interactions necessary for the assembly of the eggcase – the elucidation of the biomolecular structure and protein sequence would be essential in furthering the understanding of the molecular assembly and the process leading to the nanolattice architecture. As the focus of this dissertation work is on the collagenous mid-layer, subsequent subchapters on the background of chondrichthyan eggcases would not cover the extensive investigations in the biochemistry and secretion of the cuticles.

1.3 BIOCHEMISTRY OF ELASMOBRANCH EGGCASES

Collagen in connective tissues, such as skin, tendon, and bladder contributes high modulus elasticity and tear resistance to the material[34]. In inorganic matrices, collagen has been found in calcium-based matrices such as in bone[35], fish scales[36,37], and even corals[38]. Although the biochemistry behind elasmobranch eggcases has been investigated, conclusive evidence of its collagenous nature was provided with wide-angle X-ray scattering indicating 2.9 Å corresponding to the rise-per-residue of collagen. Characteristic of this protein structure is the consensus $(GXY)_n$ sequence, where X and Y are predominantly prolines and hydroxyprolines respectively. Therefore, the relatively high glycines, prolines, and hydroxyprolines seen in amino acid analyses agree with the proposed collagenous nature of the dogfish eggcase.

The most abundant collagen, Type I collagen, belongs to the family of fibril-forming collagens. As a whole, fibril-forming collagens, including Type II, III, V, XI, and XXIV, constitutes 80 – 90% of all collagen found in *Homo sapiens* with the remaining belonging to network-forming, anchoring fibrils, fibril-associated collagens with interrupted triple helices (FACIT), membrane-associated collagens with interrupted triple helices (MACIT), and multiple triple-helix domains and interruptions (MULTIPLEXIN) collagen[39,40]. A characteristic feature of all collagens is the formation of a right-handed superhelix comprising of three staggered left-handed polyproline II helices[39]. In type I collagen, these superhelices are aligned in a quarter-staggered fashion that gives rise to fibers with distinctive *d-spacings* observed in tendon under transmission electron microscopy[40]. These *d-spacings* originate from the gaps and overlaps formed due to the quarter staggering. Conversely, and of particular interest due to the relevance to the swell shark egg case, network forming collagen type IV, and VIII could oligomerize in antiparallel orientations followed by interactions via chain ends to form networks[41,42].

Collagen molecules are typically high in molecular weight, intimately intertwined with neighboring microfibrils, and heavily cross-linked. This leads to difficulty in isolating and characterizing the structural collagenous proteins involved in formation of the eggcase. Edman sequencing of pepsinized and trypsinized peptides of the nidamental gland extract resulted in a partial protein sequence that showed similarities to collagen type X, IV and VI. However, the identified similar sequences were in essence the consensus $(GXY)_n$ collagen sequence which has high homology across all collagenous protein. These matches had an identity of at least 30% owing to the conserved glycines. Additionally, the sparse coverage does not sufficiently inform on the protein structure of the non-collagenous (NC) end domains. The NC end domains are crucial components for higher-order self-assembly of collagens and distinguishes the various types of collagen[43]. Nonetheless, it is compelling to consider the similarity with collagen type X as both type VIII and X collagens form non-stochastic hexagonal collagenous networks[44,45], comparable to the tetragonal networks of chondrichthyan eggcases.

The toughness, high thermal shrinkage temperature, insolubility and resistance to bacterial and enzymatic degradation agrees with a heavily crosslinked structure[22,27]. Arnow staining of hydrolysates and proteins extracted from freshly laid little skate, *Raja erinacea*, eggcases indicated the presence of catechol moieties in the eggcase[46,47]. This is in agreement with the proposed quinone-tanning of chondrichthyan eggcases inferred from nidamental gland staining[22,25]. Solubility of proteins in the little skate eggcase was also seen to inversely correlate with amounts of detected catechol moieties in hydrolysates — with freshly secreted capsular material of a partially formed eggcase containing the least catechols and the most in the tanned regions of the partially formed eggcase[47]. Similarly, the amount of tyrosine inversely correlates with the amount of catechol moieties in the partially formed eggcase. This suggests that the quantified catecholic moieties arises from DOPA residues and are post-translationally modified from tyrosine. However, the results do not preclude the presence of protected small molecule catechols being involved in the tanning process. Sulfhydryl crosslinks have also been seen to play an important role in maintaining protein insolubility, where some proteins are only solubilized from freshly secreted eggcase upon treatment by dithiothreitol under denaturing conditions[47].

Neutral sugars were also detected in eggcase hydrolysates. Although there is no clear distinction between the cuticles and the collagenous mid-layer[18], periodic acid-Schiff (PAS) staining of the nidamental gland supports the hypothesis of the co-secretion of saccharides with the collagenous proteins[18,25]. PAS staining of the dogfish eggcase indicated that the saccharides are primarily localized between the interface of the outer cuticle and the collagenous mid-layer[25]. Therefore, existing knowledge on chondrichthyan eggcases has established that the collagenous mid-layer comprising the unique nanolattice architecture is composed of collagenous proteins, stabilized by sulfhydryl and DOPA crosslinks, and possibly having a matrix composed of glycosylated proteins.

1.4 SELF-ASSEMBLY OF ELASMOBRANCH EGGCASES

Optical anisotropy arising from the highly ordered ultrastructure is apparent from the significant birefringence observed under polarized optical microscopy[48]. Despite modern innovations, ordered soft materials such as block-copolymers rely on relatively high temperatures during processing. Therefore, it is noteworthy to emphasize that the secretion and processing of the highly ordered eggcase are constrained by biologically relevant aqueous conditions where extreme pH, temperatures, and pressure are impossible to achieve and incompatible with living tissue. In general, dense biological materials can be secreted as coacervates, or as a liquid crystalline (LC) phase. The latter is seen in the secretion of highly ordered materials like tendon, mussel byssus, and silk[49–51].

TEM observation of the dogfish nidamental gland confirms the formation of various lyotropic LC phases within secretory granules found in the D-zone which secretes the collagenous mid-layer[52]. The functional unit of the D-zone consists of a secretory tubule, secretory duct, a spinneret containing baffle plates, and the transverse groove. In each half of the gland, ~150 secretory tubules in a single row converge into a single transverse groove. The gland is composed of ~30 of the transverse grooves which gives rise to the laminated structure of the dogfish eggcase. Distinct LC phases were observed throughout the six secretion stages — (1) assembly of collagen, (2) formation of granules, (3) maturation of granules, (4) coalescence of granules in the lumen of the glandular tubule, (5) initiation of fibrillogenesis during transportation of coalesced fibril through the duct and spinneret, followed by (6) formation of the capsule. Stage 1 to 3 exists within granules that are ~2 µm in the secretory cells, while stage 4 to 6 exists in the lumen.[52]

The LC phases — isotropic, lamellar, micellar, cholesteric, hexagonal columnar, and the highly ordered nanolattice — were observed under TEM of the nidamental gland. The observed transitions in the LC phases were distinguished between, during the formation and maturation of granules, merocrine secretion, and fibrillogenesis. During the formation and maturation of granules, isotropic, micellar, lamellar, cholesteric, and hexagonal columnar phases were observed with increasing distance from the endoplasmic reticulum. The cholesteric and hexagonal phases were observed to coexist at the apex of the cell during merocrine secretion followed by transitions back to lamellar and micellar phases upon exocytosis and coalescence in the lumen of the tubule. The lamellar phase was seen to undergo transitions to an inverse micellar (hydrophobic center) and a micellar (hydrophilic center) phase as it migrates towards the transverse groove. Finally, within and beyond the grooves, a phase corresponding to the highly ordered nanolattice structure was observed[52]. Further investigations of the pH variations within the nidamental gland elucidated an increasingly neutral pH as the granules are being secreted. Isolated granules exposed to a range of pH seemingly agree with the phases observed within the nidamental gland, and that the final nanolattice phase forms at ~ pH 8 — 9, similar to the pH beyond the transverse grooves and that of seawater. It has been proposed by the authors that acidic pH is necessary for the storage of a highly concentrated protein. This prevents premature aggregation and crosslinking due to electrostatic repulsion, while still allowing hydrophobic interactions between terminal regions to be involved in the formation of a lyotropic LC phase[53]. In summary, chondrichthyan eggcases are fabricated by encapsulating the ovum with LC precursors using an extrusion based process. Although the exact driving forces are unknown, pH is known to play a significant role in the assembly process of the collagenous mid-layer that comprises a highly ordered nanolattice architecture.

1.5 MOTIVATION AND THESIS OUTLINE

Nature has evolved billions of years to develop multiphase materials in animals and plants with complex hierarchical ordering that have proven advantageous at certain points in an organism's evolutionary history[54,55]. An admirable aspect of these highly intricate materials is that the synthesis and fabrication are not only constrained by the available building blocks – amino acids, saccharides, and environmentally obtainable minerals – but also by temperature, solvent conditions, and pressure. In comparison to synthetic materials, these biological materials often have the advantage of being lightweight, multi-functional, and biodegradable.

The chondrichthyan eggcase has proven to be a compelling model system for tough yet permeable membranes. While toughness and porosity are typically mutually exclusive, chondrichthyan eggcases have adapted a hierarchically ordered structure — comprising a collagenous nanolattice network that permits selective permeability while ensuring mechanical toughness. The studies detailed within this dissertation aim to further the understanding of the multi-functional swell shark eggcase, a chondrichthyan that is endemic to the central coast of California.

Understanding the underlying structural adaptations in these eggcases would provide insights into novel toughening strategies. This would be advantageous to the development of materials where both strength and permeability are desirable such as multifunctional fiber-reinforced soft composites[56], mechanical metamaterials[57], and ultrafiltration membranes[58]. Additionally, owing to its highly ordered ultrastructure and LC-driven assembly, the eggcase has been previously touted to be nature's rendition of a liquid crystalline elastomer (LCE)[49]. The molecular design principles of the eggcase self-assembly strategy would provide a new paradigm for the processing and fabrication of LCEs, metamaterials, and membranes.

In Chapter 2, structural adaptations of the swell shark eggcase and how these correlate to the excellent mechanical properties were elucidated using electron microscopy and X-ray scattering. Key to the findings was a stepwise cumulative deformation mechanism, as well as lattice-governed deformation mechanisms such as the formation of uniform shear bandings and lattice rotation. In Chapter 3, leveraging proteomic and transcriptomic techniques, we identified a novel family of proteins involving protein domains classically associated with the immune system. Structurally homologous proteins were also found in the genomes of oviparous and ovoviviparous chondrichthyans. The sequence predicted molecular structure of which could rationalize the formation of the LC phases that were observed in the nidamental glands of the related dogfish. Finally, in

Chapter 5, we conclude with a summary of our discoveries and the potential implications in bio-inspired materials, and the furthering of understanding of biological materials.

1.6 REFERENCES

1. Cuomo, S. The Sinews of War: Ancient Catapults. *Science* **303**, 771–772 (2004).
2. Berkson, J. & Shuster, C. N. The Horseshoe Crab: The Battle for a True Multiple-use Resource. *Fisheries* **24**, 6–10 (1999).
3. Hwang, J. *et al.* Biomimetics: forecasting the future of science, engineering, and medicine. *Int. J. Nanomedicine* **10**, 5701–5713 (2015).
4. Bixler, G. D. & Bhushan, B. Fluid Drag Reduction with Shark-Skin Riblet Inspired Microstructured Surfaces. *Adv. Funct. Mater.* **23**, 4507–4528 (2013).
5. Carman, M. L. *et al.* Engineered antifouling microtopographies – correlating wettability with cell attachment. *Biofouling* **22**, 11–21 (2006).
6. Smith, B. L. *et al.* Molecular mechanistic origin of the toughness of natural adhesives, fibres and composites. *Nature* **399**, 761–763 (1999).
7. Lee, B. P., Messersmith, P. B., Israelachvili, J. N. & Waite, J. H. Mussel-Inspired Adhesives and Coatings. *Annu. Rev. Mater. Res.* **41**, 99–132 (2011).
8. Waite, J. H. Mussel adhesion – essential footwork. *J. Exp. Biol.* **220**, 517–530 (2017).
9. Filippidi, E. *et al.* Toughening elastomers using mussel-inspired iron-catechol complexes. *Science* **358**, 502–505 (2017).
10. Holten-Andersen, N. *et al.* pH-induced metal-ligand cross-links inspired by mussel yield self-healing polymer networks with near-covalent elastic moduli. *Proc. Natl. Acad. Sci.* **108**, 2651–2655 (2011).
11. Miserez, A., Wasko, S. S., Carpenter, C. F. & Waite, J. H. Non-entropic and reversible long-range deformation of an encapsulating bioelastomer. *Nat. Mater.* **8**, 910–916 (2009).
12. Wasko, S. S. *et al.* Structural Proteins from Whelk Egg Capsule with Long Range Elasticity Associated with a Solid-State Phase Transition. *Biomacromolecules* **15**, 30–42 (2014).
13. Walker, A. A., Weisman, S., Kameda, T. & Sutherland, T. D. Natural Templates for Coiled-Coil Biomaterials from Praying Mantis Egg Cases. *Biomacromolecules* **13**, 4264–4272 (2012).
14. Rapoport, H. S. & Shadwick, R. E. Mechanical Characterization of an Unusual Elastic Biomaterial from the Egg Capsules of Marine Snails (Busycon spp.). *Biomacromolecules* **3**, 42–50 (2002).
15. Cornet, V. *et al.* How Egg Case Proteins Can Protect Cuttlefish Offspring? *PLOS ONE* **10**, e0132836 (2015).
16. Kodali, V. K. *et al.* A Novel Disulfide-Rich Protein Motif from Avian Eggshell Membranes. *PLOS ONE* **6**, e18187 (2011).
17. Kawasaki, H., Sato, H. & Suzuki, M. Structural Proteins in the silkworm egg-shells. *Insect Biochem.* **1**, 130–148 (1971).
18. Rusaouën, M., Pujol, J.-P., Bocquet, J., Veillard, A. & Borel, J.-P. Evidence of collagen in the egg capsule of the dogfish, scyliorhinus canicula. *Comp. Biochem. Physiol. Part B Comp. Biochem.* **53**, 539–543 (1976).

19. Knight, D. P. & Hunt, S. Fibril structure of collagen in egg capsule of dogfish. *Nature* **249**, 379–380 (1974).
20. Hornsey, D. J. Permeability coefficients of the egg-case membrane ofScyliorhinus canicula L. *Experientia* **34**, 1596–1597 (1978).
21. Mancusi, C. *et al.* An identification key for Chondrichthyes egg cases of the Mediterranean and Black Sea. *Eur. Zool. J.* **88**, 436–448 (2021).
22. Knight, D. P., Feng, D. & Stewart, M. Structure and Function of the Salachian Egg Case. *Biol. Rev.* **71**, 81–111 (1996).
23. Ehrlich, H. *Biological Materials of Marine Origin: Vertebrates*. (Springer Netherlands, 2015). doi:10.1007/978-94-007-5730-1.
24. Knight, D. P. & Feng, D. Interaction of collagen with hydrophobic protein granules in the egg capsule of the dogfish scyliorhinus canicula. *Tissue Cell* **26**, 155–167 (1994).
25. Feng, D. & Knight, D. P. Secretion and stabilization of the layers of the egg capsule of the dogfish Scyuorhinus canicula. *Tissue Cell* **24**, 773–790 (1992).
26. Iconomidou, V. A. *et al.* Dogfish egg case structural studies by ATR FT-IR and FT-Raman spectroscopy. *Int. J. Biol. Macromol.* **41**, 102–108 (2007).
27. Hunt, S. The Selachian Egg Case Collagen. in *Biology of Invertebrate and Lower Vertebrate Collagens* (eds. Bairati, A. & Garrone, R.) 409–434 (Springer US, 1985). doi:10.1007/978-1-4684-7636-1_36.
28. BROWN, C. H. Egg-capsule Proteins of Selachians and Trout. *J. Cell Sci.* **s3-96**, 483–488 (1955).
29. Gathercole, L. J., Atkins, E. D. T., Goldbeck-Wood, E. G. & Barnard, K. Molecular bending and networks in a basement membrane-like collagen: packing in dogfish egg capsule collagen. *Int. J. Biol. Macromol.* **15**, 81–88 (1993).
30. Knupp, C., Chew, M., Morris, E. & Squire, J. Three-Dimensional Reconstruction of a Collagen IV Analogue in the Dogfish Egg Case Wall. *J. Struct. Biol.* **117**, 209–221 (1996).
31. Knupp, C. & Squire, J. X-Ray Diffraction Analysis of the 3D Organization of Collagen Fibrils in the Wall of the Dogfish Egg Case. *Proc. Biol. Sci.* **265**, 2177–2186 (1998).
32. Knight, D. P. & Hunt, S. A kinked molecular model for the collagen-containing fibrils in the egg case of the dogfish Scyliorhinus caniculus. *Tissue Cell* **18**, 201–208 (1986).
33. Knupp, C., Chew, M. & Squire, J. Collagen Packing in the Dogfish Egg Case Wall. *J. Struct. Biol.* **122**, 101–110 (1998).
34. Yang, W. *et al.* On the tear resistance of skin. *Nat. Commun.* **6**, 6649 (2015).
35. Viguet-Carrin, S., Garnero, P. & Delmas, P. D. The role of collagen in bone strength. *Osteoporos. Int.* **17**, 319–336 (2006).
36. Zimmermann, E. A. *et al.* Mechanical adaptability of the Bouligand-type structure in natural dermal armour. *Nat. Commun.* **4**, 2634 (2013).
37. Quan, H., Yang, W., Schaible, E., Ritchie, R. O. & Meyers, M. A. Novel Defense Mechanisms in the Armor of the Scales of the “Living Fossil” Coelacanth Fish. *Adv. Funct. Mater.* **28**, 1804237 (2018).
38. Ehrlich, H. *et al.* Mineralization of the metre-long biosilica structures of glass sponges is templated on hydroxylated collagen. *Nat. Chem.* **2**, 1084–1088 (2010).

39. Shoulders, M. D. & Raines, R. T. Collagen Structure and Stability. *Annu. Rev. Biochem.* **78**, 929–958 (2009).
40. Ricard-Blum, S. The Collagen Family. *Cold Spring Harb. Perspect. Biol.* **3**, a004978 (2011).
41. Birk, D. E. & Brückner, P. Collagens, Suprastructures, and Collagen Fibril Assembly. in *The Extracellular Matrix: an Overview* (ed. Mecham, R. P.) 77–115 (Springer, 2011). doi:10.1007/978-3-642-16555-9_3.
42. Stephan, S., Sherratt, M. J., Hodson, N., Shuttleworth, C. A. & Kielty, C. M. Expression and Supramolecular Assembly of Recombinant α1(VIII) and α2(VIII) Collagen Homotrimers*. *J. Biol. Chem.* **279**, 21469–21477 (2004).
43. Luong, T.-T., Boutillon, M.-M., Garrone, R. & Knight, D. P. Characterization of Selachian Egg Case Collagen. *Biochem. Biophys. Res. Commun.* **250**, 657–663 (1998).
44. Bogin, O. *et al.* Insight into Schmid Metaphyseal Chondrodysplasia from the Crystal Structure of the Collagen X NC1 Domain Trimer. *Structure* **10**, 165–173 (2002).
45. Kvansakul, M., Bogin, O., Hohenester, E. & Yayon, A. Crystal structure of the collagen α1(VIII) NC1 trimer. *Matrix Biol.* **22**, 145–152 (2003).
46. Koob, T. J. & Cox, D. L. Introduction and oxidation of catechols during the formation of the skate (Raja erinacea) egg capsule. *J. Mar. Biol. Assoc. U. K.* **70**, 395–411 (1990).
47. Koob, T. J. & Cox, D. L. Stabilization and sclerotization of Raja erinacea egg capsule proteins. in *The reproduction and development of sharks, skates, rays and ratfishes* (eds. Demski, L. S. & Wourms, J. P.) 151–157 (Springer Netherlands, 1993). doi:10.1007/978-94-017-3450-9_13.
48. Knight, D. P. *et al.* Molecular orientations in an extruded collagenous composite, the marginal rib of the egg capsule of the dogfish Scyliorhinus canicula; a novel lyotropic liquid crystalline arrangement and its origin in the spinnerets. *Philos. Trans. R. Soc. Lond. B. Biol. Sci.* **351**, 1205–1222 (1996).
49. Knight, D. P. & Vollrath, F. Biological liquid crystal elastomers. *Philos. Trans. R. Soc. Lond. B. Biol. Sci.* **357**, 155–163 (2002).
50. W. Hamley, I. Liquid crystal phase formation by biopolymers. *Soft Matter* **6**, 1863–1871 (2010).
51. Harrington, M. J. & Waite, J. H. pH-Dependent Locking of Giant Mesogens in Fibers Drawn from Mussel Byssal Collagens. *Biomacromolecules* **9**, 1480–1486 (2008).
52. Knight, D. P., Feng, D., Stewart, M. & King, E. Changes in macromolecular organization in collagen assemblies during secretion in the nidamental gland and formation of the egg capsule wall in the dogfish Scyliorhinus canicula. *Philos. Trans. R. Soc. Lond. B. Biol. Sci.* **341**, 419–436 (1993).
53. Feng, D. & Knight, D. P. The effect of pH on fibrillogenesis of collagen in the egg capsule of the dogfish, Scyliorhinus canicula. *Tissue Cell* **26**, 649–659 (1994).
54. Wegst, U. G. K. & Ashby, M. F. The mechanical efficiency of natural materials. *Philos. Mag.* **84**, 2167–2186 (2004).
55. Liu, Z., Zhang, Z. & Ritchie, R. O. On the Materials Science of Nature's Arms Race. *Adv. Mater.* **30**, 1705220 (2018).

56. King, D. R. *et al.* Extremely tough composites from fabric reinforced polyampholyte hydrogels. *Mater. Horiz.* **2**, 584–591 (2015).
57. Bauer, J. *et al.* Nanolattices: An Emerging Class of Mechanical Metamaterials. *Adv. Mater.* **29**, 1701850 (2017).
58. Landsman, M. R. *et al.* Water Treatment: Are Membranes the Panacea? *Annu. Rev. Chem. Biomol. Eng.* **11**, 559–585 (2020).

2 NANOLATTICED ARCHITECTURE MITIGATES DAMAGE IN SHARK EGGCASES

Structural versatility and multifunctionality of biological materials have resulted in countless bioinspired strategies seeking to emulate the properties of nature. The nanostructured eggcase of swell sharks is one of the toughest permeable membranes known and hence, presents itself as a model system for materials where the conflicting properties — strength and porosity — are desirable. The eggcase possesses an intricately ordered structure that is designed to protect delicate embryos from the external environment while enabling respiratory and metabolic exchange, achieving a tactical balance between conflicting properties. Herein, structural analyses revealed an enabling nanolattice architecture that constitutes a Bouligand-like nanoribbon hierarchical assembly. The three distinct hierarchical architectural adaptations enhance eggcase survival: Bouligand-like organization for in-plane isotropic reinforcement, non-cylindrical nanoribbons maximize interfacial stress distribution, and highly ordered nanolattices enable permeability and lattice-governed toughening mechanisms. These discoveries provide fundamental insights for the improvement of multifunctional membranes, fiber-reinforced soft composites, and mechanical metamaterials.

2.1 INTRODUCTION

Nature has no equal in its ability to achieve multiple high-performance capabilities within the same material. Eggshells and eggcases are eloquent examples of multifunctional, protective structural materials[1–3]. Unlike the brittle eggshells of avian eggs, egg-laying elasmobranchs, such as sharks and skates, have evolved to produce leathery eggcases that allow the delicate embryos to survive in unrelentingly turbulent subtidal environments. The collagenous nature of elasmobranch eggcases has been well established by X-ray scattering and amino acid analyses[4,5]. Like tendon collagen, the ultrastructure of elasmobranch eggcases reveals an intricately ordered hierarchical structure spanning multiple lengthscales. However, the similarity to tendon collagen diverges at the nanoscale, where an exquisite permeable tetragonal network — resembling mechanical metamaterials — distinguishes the collagenous eggcase assembly[4]. Understanding the structural adaptations in these eggcases would provide insights into toughening strategies that would be of broad utility to the development of multifunctional soft composites[6], ultrafiltration membranes[7,8], and mechanical metamaterials[9].

2.2 RESULTS AND DISCUSSION

It is widely recognized that biochemical and ultrastructural adaptations play a crucial role in providing excellent energy absorbing properties and selective permeability mandatory for the survival of vulnerable embryos. Here, we describe how elaborate structural adaptations relate to mechanical properties in the eggcase of the swell shark, *Cephaloscyllium ventriosum*, an egg-laying (oviparous) elasmobranch endemic to the coast of central California. Despite a hydration of ~68% (w/w) water and density of 1.06 g/cm^3, recent investigations into the mechanical properties of swell shark eggcase have found it to have an impressive work to failure (W_f) of 10.7 ± 1.0 MJ/m^3, twice that of tendon and fiberglass. Normalized by its density, the eggcase has a W_f of approximately 4 times greater than steel[10]. In comparison with recent innovations in strong and tough soft composites, the eggcase has an ultimate tensile strength of 25.4 ± 1.4 MPa exceeding that of double-network hydrogels and fiber-reinforced soft composites[6,11] (Fig. A1). This is in conjunction with the eggcase's initial modulus of 107.9 ± 8.3 MPa and a strain to failure of 0.66 ± 0.04.

Key to the ability of the swell shark eggcase to serve as a selective filtration membrane for gaseous and metabolic waste exchange is its inherent porosity. In practice, porosities frequently lead to lower modulus and toughness – a trade-off that needs to be tactically balanced for permeable protective structures. Through a combination of microscopy and *in-situ* small angle X-ray scattering (SAXS) during tensile deformation, we have identified structural adaptations and deformation mechanisms that are responsible for toughening the porous eggcase.

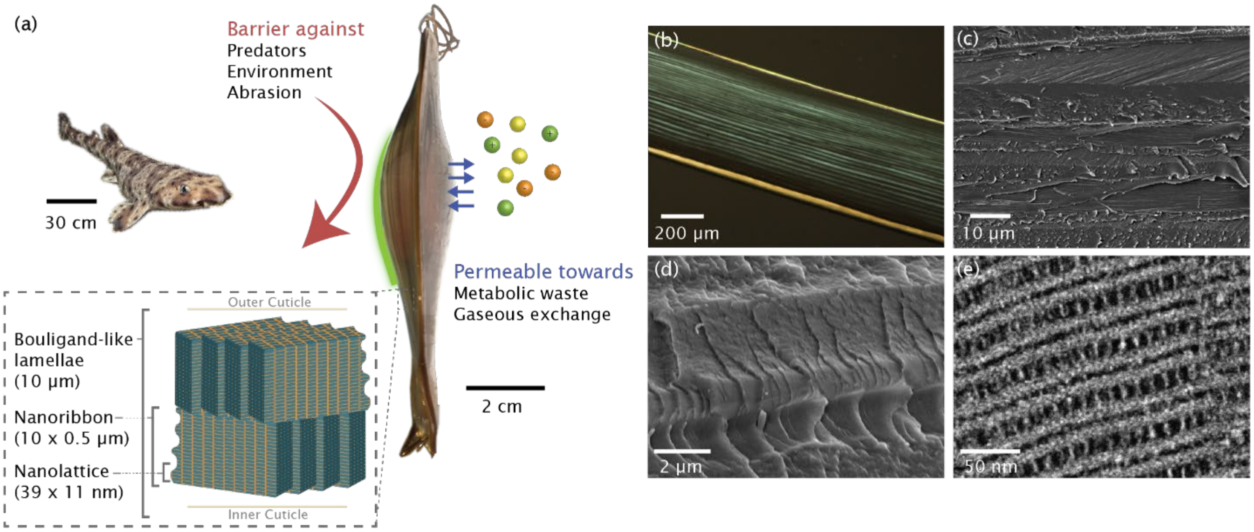

Fig. 2.1. Hierarchical structure of the eggcase integrates both permeability and toughness. (a) Multifunctionality of eggcases ensures the survival of developing embryos. Inset illustrates the characteristic architectures of the eggcase. (b) Birefringence of the eggcase cross-section observed under polarized optical microscopy. Scanning electron microscopy (SEM) images of (c) cryo-sectioned eggcase showing lamellae of unidirectional fibers with a ~30˚ rotation per layer and (d) freeze-fractured eggcase emphasizing the non-cylindrical aspect of the fibers (nanoribbons). (e) High magnification TEM image of the eggcase showing structured tetragonal pores within nanoribbons.

Our structural analyses of eggcase using electron microscopy and SAXS revealed a hierarchically ordered structure from the micro- down to nanometer length scales (Fig. 2.1). At the microscale, the eggcase has a multi-ply lamellar organization with lamellae that are composed of single rows of unidirectional non-cylindrical fibers (nanoribbons). These nanoribbons have ~30˚ interlamellar rotation which gives rise to a Bouligand-like mesophase, providing the eggcase with in-plane isotropic mechanical reinforcement and crack bridging[12,13]. The nanoribbon geometry provides an advantageous surface area to volume ratio that is 2.65 times larger than cylinders of equivalent volume (appendix A). Ostensibly, the nanoribbons have been adapted to maximize stress distribution and energy transfer across the composite components[14]. At higher magnifications, ultrathin sections of the eggcase viewed under transmission electron microscopy (TEM) exhibited a highly ordered, pseudo-crystalline, tetragonal network that forms the nanoribbons — analogous to nanolattice mechanical metamaterials[9].

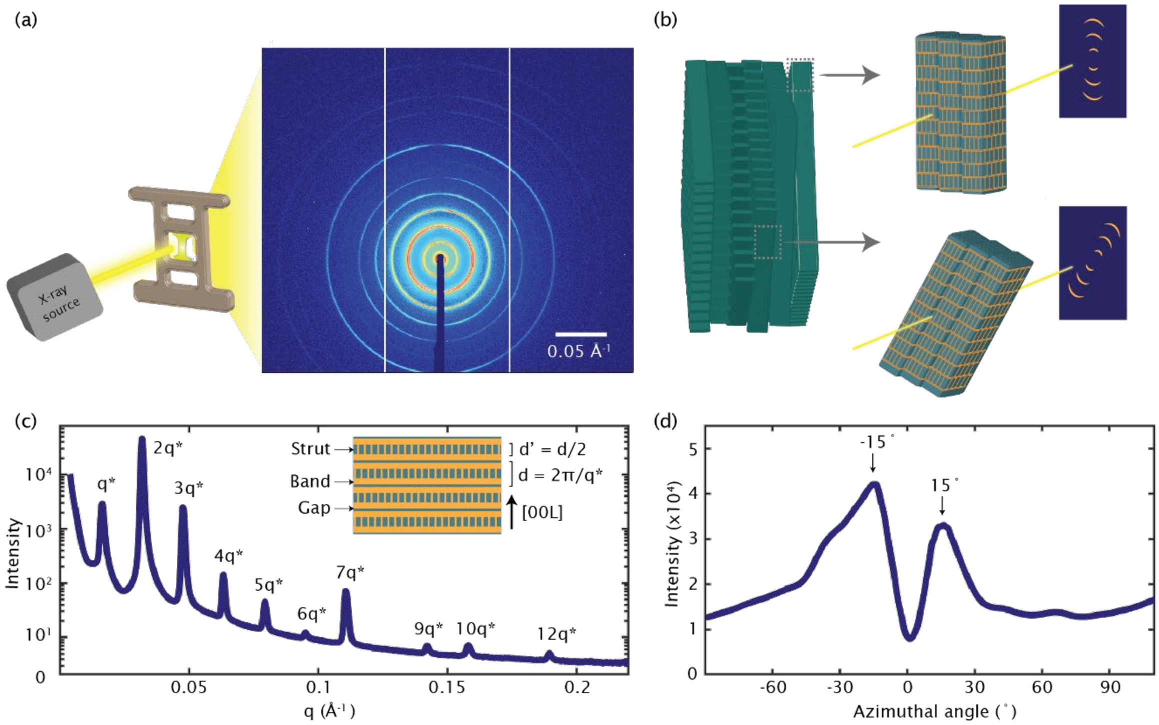

Fig. 2.2 Synchrotron SAXS of the eggcase. (a) Experimental set up for in-situ SAXS during tensile deformation and the corresponding 2D SAXS of an unstrained sample. (b) Illustration of nanolattice within a nanoribbon and the corresponding through-plane SAXS pattern. (c) Radial integration of 2D SAXS pattern with a representative schematic of superlattice morphology (inset). (d) Azimuthal integration of 2q*, as the *d*-periods are oriented along the long axis of the nanoribbons.

Through-plane SAXS reflections are consistent with a layered structure where q/q* = 1, 2, 3… with q* being the primary peak arising from the 39 nm spacings – corresponding with TEM observations (Fig. 2.2c). The exceptional order of the nanolattices was apparent in SAXS with reflections persistent up to the 12th order. The absence of SAXS peaks corresponding to the struts in the through-plane diffraction could be due to swelling of the struts or material around the struts influencing the electron density contrast, an increase in flexibility and mobility due to being in a hydrated state, and overshadowing by the q* peaks of significantly higher intensity. However, weak diffraction patterns arising from the diagonal planes are observed when the samples were rotated 90˚ (on-edge) with respect to the incident beam. The presence of these peaks supports the proposed body-centered tetragonal (BCT) symmetry that has been characterized in the dogfish eggcase (Fig. A3)[15]. Intriguingly, the 2q* diffraction peak had a diffraction intensity greater than q* and the FFT of TEM images reflects a similar trend. To further investigate the origin of this, the q* and 2q* FFT peaks were masked and the corresponding inverse FFT overlayed on the TEM image (Fig. A4). The composite image emphasizes the remarkable regularity of the …ABCBAB… stacking. The nanolattice architecture bears a close resemblance to the proposed superlattice structure of charged block copolymers[16] and of oxygen-deficient perovskite derivatives[17], wherein stacking of continuous and perforated layers alternates. To the best of our knowledge, a non-mineralized superlattice natural material has never been categorically identified and would serve as a pivotal model system for non-stochastic porous structures. Immediately obvious from the diffraction pattern is the absence of discretized nanoribbon orientation, unlike collagen fibers within the *Arapaima gigas* scales [12] or in uniaxially aligned collagen fibers in tendon[18]. Azimuthal integration of the 2q* diffraction peak indicated a continuous angular distribution of nanoribbons with a preferred orientation of ±15˚ with respect to the long axis of the eggcase (Fig. 2.2d).

By observing the diffraction patterns arising from the nanolattice during *in-situ* tensile deformation and corroboration by microscopy, we were able to determine the mechanisms involved in toughening of the eggcase. Three distinct deformation regimes with stepwise degradation of modulus can be identified from the stress-strain behaviour of the eggcase, suggesting a progressive failure of subcomponents within the architecture with well-defined fracture stress or yield points. Analyses of the X-ray diffraction patterns indicate a cumulative engagement of fibers in the deformation of the eggcase. To glean additional insights into the strain distribution within the eggcase, fibrillar strains at 0˚, 45˚, and 90˚ are plotted against the sample strain (Fig. 2.3b).

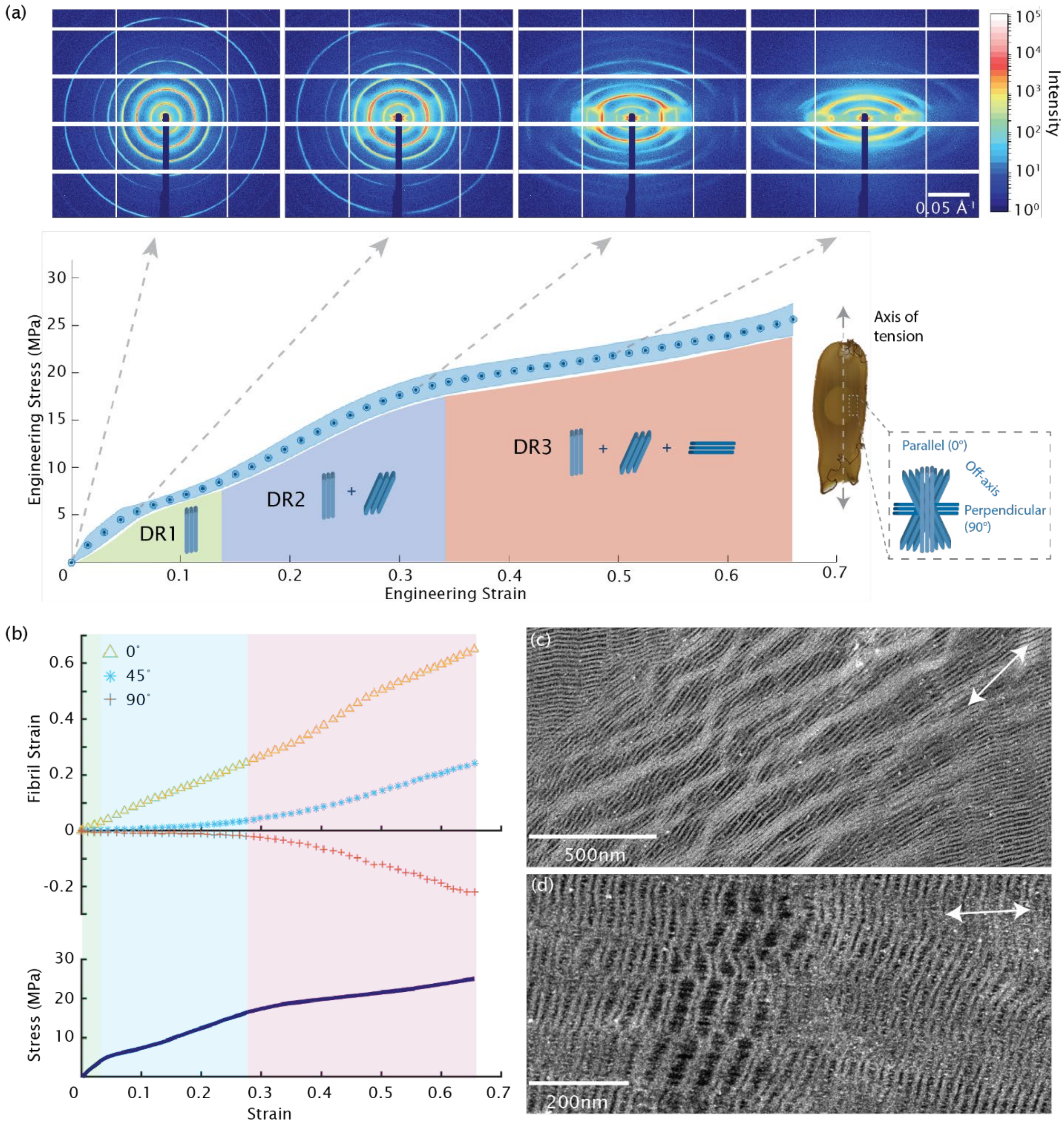

Fig. 2.3. Elucidation of deformation mechanisms using i*n-situ* SAXS during tensile deformation and TEM. (a) Stress-strain curve of swell shark eggcase with three distinct deformation regimes (DR) and corresponding SAXS patterns at ε = 0%, 5.8%, 31%, and 50%. Inset illustrates the stress axis with respect to the eggcase and nanoribbon orientations. (b) Nanoribbon strain along 0˚, 45˚ and 90˚. TEM of eggcase strained to 25% strain showing (c) shear bands and rotation of nanolattice and (d) fracture of struts. Stress axes indicated by arrows.

The 1st deformation regime involves elongation of the nanoribbons parallel to the stress axis while the 2nd regime then engaged the off-axis fibers in the deformation process. As the nanoribbons deformed in the 1st and 2nd regimes, a gradual decrease in scattering intensity and order of nanoribbons parallel to the stress axis occurred. Accordingly, the onset of the 2nd deformation regime and the consequent decrease in modulus coincided with the observations of significant reorientation and uniform shear banding in samples that were chemically fixed while strained to the 2nd regime (Fig. 2.3c). TEM micrographs of the onset of shear bands suggest that failure primarily happened along the planes of lowest density – along the struts and gap region. In all cases, the long axes of the shear bands were oriented along the macroscopic tensile axis. Consideration of the formation of shear bands within a simplified anisotropic model[19] agrees with the observed directions of the shear bands and supports the eventual formation of the diamond-shaped damage zones (Fig. A5) seen in the egg case (appendix A). Such features resemble the toughening mechanism seen in metallic glass composites that facilitates uniform nucleation and distribution of shear bands. This prevents the formation of critical strain localization, leading to an overall increase in ductility[20]. Additionally, lattice reorientation of up to 65˚ was also observed with weak planes preferentially reoriented parallel to the stress axis, facilitating shear deformation along susceptible planes. Reorientations were independent of nanoribbon orientation as seen by isolated islands of reoriented nanolattices while the reorientation preference is indicative of a deformation mechanism that is governed by lattice asymmetry (Fig. A5). Consequent of the geometric softening mechanisms, higher strains could be accommodated by the nanoribbons thereby toughening the eggcase.

In the 3rd regime, nanoribbons perpendicular to the stress axis shortened due to Poisson's effect arising from strain perpendicular to the nanoribbon axis. Simultaneous compressive forces from Poisson's contraction of adjacent lamellae could additionally contribute to the effective shortening of the nanoribbons[12]. At the same time, an increase in diffraction intensity parallel to the stress axis was observed implying an increase in nanolattice alignment. The increase in scattering intensity at q* was significantly more than at 2q*, suggesting a disruption of the hierarchical superlattice and is supported by the increasingly disordered structure seen by TEM (Figs. A6, A7). Conversely, the intensity ratio of the off-axis nanolattices remains consistent with the initial observation where 2q* is greater than q*, pointing to the conservation of the superlattice symmetry along the off-axis orientation (Fig. A6).

Examining the strain of nanoribbons parallel to the stress axis indicates a deformation rate that was similar to the macroscopic strain throughout all three regimes and to a fibrillar strain of 76 ± 6.6%. The discrepancy between fibrillar and macroscopic strain was presumed to be due to variation of strain across the sample caused by non-homogenous thickness. The comparable deformation implies that the strain in the nanoribbons parallel to the stress axis was continuous across the eggcase and that, unlike collagenous tendons[18,21] and fish scales[12], there was minimal strain on the matrix in this orientation. The ability to sustain high strains prior to failure, exceeding collagen fibril strain by ~1800%[18,21], can be attributed to the tetragonal architecture within the nanoribbon. Besides lattice-governed shear banding and reorientation, presence of porosities minimize constraints by the surrounding materials during deformation while acting as stress concentrators that provide multiple nucleation sites for crack propagation (Fig. 2.3d)[22]. The struts act as effective crack bridges and given the nanoscale architecture of the lattice, exploitation of size-dependent material strengthening effects at the nanometer length-scale would, in principle, improve flaw insensitivity as well[9,23–25]

2.3 CONCLUSION

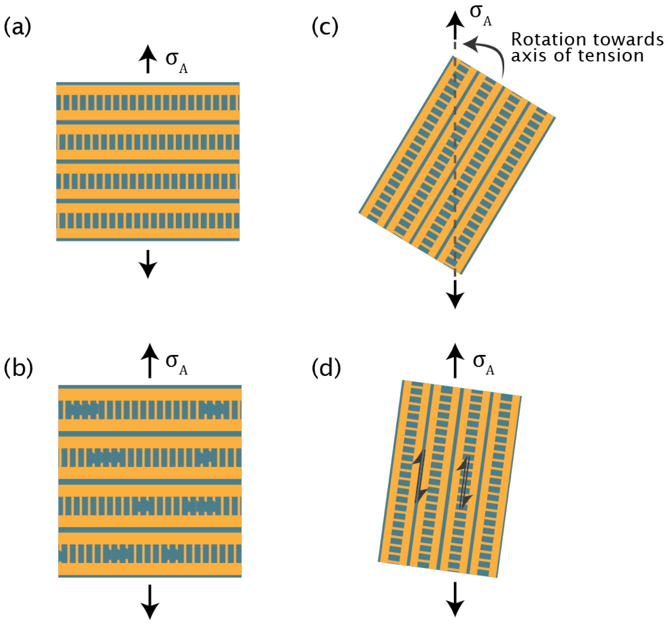

Fig. 2.4. Deformation mechanisms seen in the nanolattice architecture from *in-situ* SAXS during tensile deformation and TEM. (a) Distortion of nanolattice architecture, (b) fracturing of struts, (c) rotation, and (d) nucleation of shear bands along weak planes with σ_A being the applied stress.

In conclusion, swell shark eggcases showcase extensive structural adaptions and unique deformation processes in a highly intricate hierarchical architecture. In our work, we have identified a Bouligand-like architecture that provides in-plane isotropic mechanical reinforcement, acylindrical nanoribbons optimized for effective stress distribution, and an exceptionally ordered nanolattice architecture that gives rise to lattice-governed toughening mechanisms while permitting selective permeability. The most notable discoveries are a cumulative deformation mechanism that involves a stepwise engagement of nanoribbons of different orientations, and lattice-governed toughening mechanisms that facilitates plasticity (Fig. 2.4). The asymmetry and reorientation of the nanolattice make possible the uniform formation of multiple non-critical shear bands, as seen in the toughening of metallic glass composites[20]. Disruption of the superlattice symmetry only at high strains suggests a critical yield-point of a substructure within the lattice. Although impossible at this time to resolve the exact substructure, the stepwise deformation of the nanolattice serves as an effective toughening mechanism by giving rise to hidden lengths when disrupted, a common strategy in biological materials[26] and novel synthetic elastomers[27]. Despite a decrease in stiffness at higher strains due to geometric softening effects, the combination of cumulative nanoribbon engagement and lattice-governed toughening mechanisms gives rise to strain hardening and a high strain to failure. Given the impressive toughness despite porosity and high water content, the swell shark eggcase merits further scrutiny and offers timely inspiration for improved multifunctional membranes and mechanical metamaterials.

2.4 MATERIALS AND METHODS

Eggcase collection and preparation

Eggcases were harvested from both wild and tank reared swell sharks. Selection was biased towards eggcases without visible developing embryos and eggcases from tank reared sharks that were laid within 1 to 3 months. The embryos were carefully removed from the eggcase and euthanized with an overdose of MS-222 by immersion into sodium bicarbonate buffered MS-222 bath (1g/L). The procurement of eggcases is in accordance with Institutional Animal Care and Use Committee (IACUC) guidelines and reviewed by UCSB IACUC. Dogbone-shaped tensile specimens with a gauge length of 5 mm and width of 2 mm were punched from the walls of the eggcase, stored on ice, and used within 3 days.

Density and water content measurements

Eggcases were cut into pieces that are ~1 mm and dialyzed against MilliQ water for 3 times, 30 minutes each. Excess water was wicked away using paper towels and the sample was weighed (6.16g). The sample was then transferred into a measuring cylinder partially filled with MilliQ water. The displaced water was then weighed, and the displaced volume was approximated by using the known density of water at 25˚C (997 kg/m^3). The sample was lyophilized for 2 days and the water content was calculated by comparing the weight of the sample before and after lyophilization.

Polarized light microscopy sample preparation

Sample was cryosectioned to 50 µm with a cryostat (Leica CM1850) and resuspended in MilliQ water to remove residual OCT compound. Sections were examined under an optical microscope (Olympus BX51) coupled with cross polarizers (BX-POL) and imaged using a colored camera (Olympus DP73).

Macroscopic sample strain measurements

Samples were marked with a pair of permanent marker lines along the gauge length for optical strain tracking. The strain progressions were recorded via a phone camera (microscopy sample preparation) or frame-by-frame by a charge-coupled device camera (*in-situ* SAXS). The macroscopic sample strains (ε) were then determined by the change in centroid-to-centroid distance (Δl) of the marked lines with respect to the initial distance (l_0) using the equation $\varepsilon = \Delta l/l_0$. A total of 6 samples were included in the calculation for work to failure, modulus, tensile strength, initial modulus, and strain to failure.

Electron microscopy sample preparation

Dogbone-shaped samples were uniaxially strained on the MTS Bionix 200. Samples were then securely clamped using custom 3D-printed frames and buffer exchanged in a solution of 1.5X modified MarPHEM buffer (pH 8.0, 90 mM PIPES, 37.5 mM HEPES, 3 mM $MgCl_2$ and 9% sucrose)[28] for 30 minutes at 4˚C before being chemically fixed with 2.5% glutaraldehyde (EMS #16220) and 1.5% formaldehyde (EMS #15714) in 1.5X modified MarPHEM for 2 hours at 4˚C. Subsequently, samples were dialyzed against MilliQ water 3 times for 30 minutes, 12 hours, then 30 minutes at 4˚C. Strains were preserved as no shrinkage or shortening of samples was observed when the clamps were released after fixation. Native (unstrained) samples were prepared with the same fixation procedure but without loading and clamping.

SEM samples were either cryosectioned to 50 µm with a cryostat (Leica CM1850) or freeze fractured under liquid nitrogen with a sharp blade. Cryosectioned samples were resuspended in MilliQ water to remove residual OCT compound. Samples were then dehydrated with a graded series of ethanol in water of 0%, 20%, 40%, 60%, and 100% (3 times) with 10 minutes at each step. This was followed by a gradual solvent exchange of hexamethyldisilazane in ethanol of 30%, 60% and 100% (3 times) with 10 minutes at each step. Samples were air-dried overnight prior to being sputter coated with gold and palladium. Coated samples were examined under FEI Nova Nano 650 SEM.

TEM samples were stained with 2% osmium tetroxide (EMS #19150) for 90 minutes at 4˚C, washed thrice in MilliQ water with at least 10 minutes at each step, and dehydrated with a graded series of ethanol in water of 0%, 20%, 40%, 60% and 100% (3 times) with 10 minutes at each step. This was followed by a solvent exchange with propylene oxide and gradual infiltration of EMbed 812 resin as indicated by the manufacturer's protocol. Samples were then placed in silicone molds and cured at 70˚C for 24 hours. Ultra-thin sections (50 nm) of the embedded samples were then prepared on an ultramicrotome (Leica EM UC6) with a diamond knife (Diatome) and mounted on a copper grid. Sections were then further stained with 0.6% uranyl acetate (Ted Pella #19481) in 30% ethanol at 60˚C followed by 3% lead citrate (EMS #22410). Stained samples were examined under ThermoFisher Talos G2 200X in STEM mode.

***In-situ* SAXS during tensile deformation**

Dogbone-shaped samples were uniaxially and symmetrically strained on a Linkam TST350 tensile stage at a rate of 50 µm s^{-1} during SAXS measurements at the Advanced Light Source, Beamline 7.3.3[29]. Force, x-ray scattering, and sample deformation were recorded frame-by-frame simultaneously to allow real-time measurements and correlation of measurements. The samples were kept hydrated by the addition of filtered seawater to the sample before the start of the measurements. Strain to failure measurements typically took up to 180 s, and no observable change in SAXS pattern was seen in a control experiment where no strain was applied to the sample.

Scattering data were collected on a Dectris Pilatus3 2M detector, while samples were exposed to 10 keV x-rays for 0.5 s at 2.5 s intervals. Beam center and sample-to-detector distance were calibrated with silver behenate. Calibration and all SAXS data reduction were done using the Nika package[30] on Igor Pro 8.

Nanoribbon strains were extracted from the SAXS by performing line integrations (width = 3 px) from low to high q at orientations of 0˚, 45˚, and 90˚ with respect to the stress axis. The curves were fitted with a Voigt function after subtraction of an exponential baseline using code written in Python. Strains were calculated using the peak position of the primary reflection, q* ($q = 2\pi/d$) using the following equation $\varepsilon_r = \Delta d/d_0$ where Δd is the change in d-spacings and d_0 the d-spacing of the unstrained material.

Fast Fourier Transformation (FFT) and Inverse FFT of TEM Micrographs

Fourier transforms of micrographs were performed using ImageJ's FFT and Inverse FFT functions. Prior to the Inverse FFT the contrast was adjusted and the q* and 2q*peaks were masked. Data reduction was performed with ImageJ's Radial Profile Angle, and q was reported as 1/*d*.

2.5 APPENDIX A

Surface Area-Volume ratio of nanoribbons

The dimensions of the nanoribbons were approximately 10 µm wide by 0.5 µm thick, and their surface area:volume ratio may be calculated independent of length L, as volume $V_r \cong 5L$, surface area $SA_r \cong 21L$, and $SA_r{:}V_r = 4.2$. The same argument can be made for cylindrical fibers. In this case, the radius of a volumetrically equivalent cylinder is 1.26 µm, resulting in $SA_{Cyl} = 7.9L$ and a $SA_{Cyl}{:}V_{Cyl} = 1.58$. Therefore, a flattened nanoribbon has a SA:V that is 2.65 times greater than cylindrical fibers. This translates to an improved distribution of shear forces along the nanoribbon interface and efficiency for stress transfer across the interface. Similarly, this would enhance energy dissipation mechanisms involving shear across the interface[14].

Relevance of lattice asymmetry to shear band formation

To assess the benefits of an anisotropic, porous nanostructure, we consider unidirectional, aligned bands that have a very high tensile strength in a matrix that has a relatively low shear strength. This configuration is shown in Fig. A1a and, for simplicity we consider the material to deform in plane strain. The applied stress, σ_A, is tension at an angle θ to the nanostructural bands as shown in Fig. A1. We idealize the behavior of the material by neglecting elastic deformations and assuming that the anisotropic strength of the system is governed by perfectly plastic yielding, with tensile strength parallel to the bands equal to σ_o, and a yield strength in shear for the matrix equal to τ_o. Consideration of Fig. 2.3a shows that this model is an incomplete representation of the stress-strain behavior of the swell shark egg case material, but in future work, we intend to improve the treatment by incorporating anisotropic, nonlinear elasticity, and strain hardening. Furthermore, nonlinear elasticity and plasticity are interchangeable models during proportional stressing[31], and so our plasticity treatment here is a reasonable foundation for a more complete constitutive model.

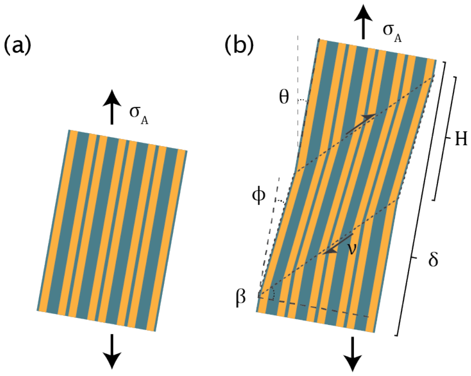

Fig. A1. Illustration of the simplified anisotropic nanostructure used in the analysis. (a) Unstrained sample and (b) strained sample with subsequent formation of shear bands.

We further assume that deformations are volume preserving at the mesoscopic level and that the yield criterion in plane strain in terms of axial and shear stress parallel to the bands is elliptical with associated plastic flow through normality. These assumptions allow us to use the results of Nizolek *et al.*[19], which entail that a perfectly plastic anisotropic material with the yield criterion we have specified will experience the formation of a shear band immediately upon yielding. Thus, when

$$\sigma_A = \frac{2\tau_o\sigma_o}{\sqrt{4\tau_o^2\cos^2 2\theta + \sigma_o^2\sin^2 2\theta}}$$

the material will both yield plastically and a shear band as shown in Fig. A1b will be generated. The angle of orientation, β, of the shear band is given by

$$\tan\beta = \frac{\sigma_o^2\tan\theta}{2(1-\tan^2\theta)\tau_o^2} + \sqrt{1 + \frac{\sigma_o^4\tan^2\theta}{4(1-\tan^2\theta)^2\tau_o^4}}$$

When the material is markedly anisotropic, say $\sigma_o/\tau_o \geq 10$, the angle β will be close to 90° even for small stress misalignments, θ, relative to the nanostructural bands. This prediction agrees with observations of shear bands in strained egg cases (Fig. 2.3c). The deformation in the band, quantified by ϕ, is such that ϕ starts at zero and increases monotonically.

Once the shear band forms and develops, the applied stress is given by Nizolek *et al.*[19] as

$$\sigma_A = \frac{\cos^2\theta\sqrt{4\tau_o^2\cos^2 2(\beta+\phi) + \sigma_o^2\sin^2 2(\beta+\phi)}}{\sin 2(\beta-\theta)}$$

while at the same time the upper end of the component shown in Fig. A1b will move vertically relative to the lower end by the distance δ given by

$$\delta = v \sin\beta = H[\tan(\beta + \phi) - \tan\beta] \sin\beta$$

We do not deduce the thickness, H, of the shear band but instead assume that it is a few times the width between neighboring nanostructural bands, as appears to be the case of the shear bands visible in Fig. 2.3c. The relatively high value of β suggests that the shear band can sustain only a moderate amount of shearing, ϕ, before deformation within the band ceases due to elastic stiffening and/or strain-hardening. This action will favor the formation of a new shear band, with the result that after a moderate amount of strain in DR2 the material becomes criss-crossed by multiple shear bands resulting in the diamond-shaped defects seen in Figs. 2.3c and A5c. A similar behavior is known to occur in conjunction with kink-bands in compression[19].

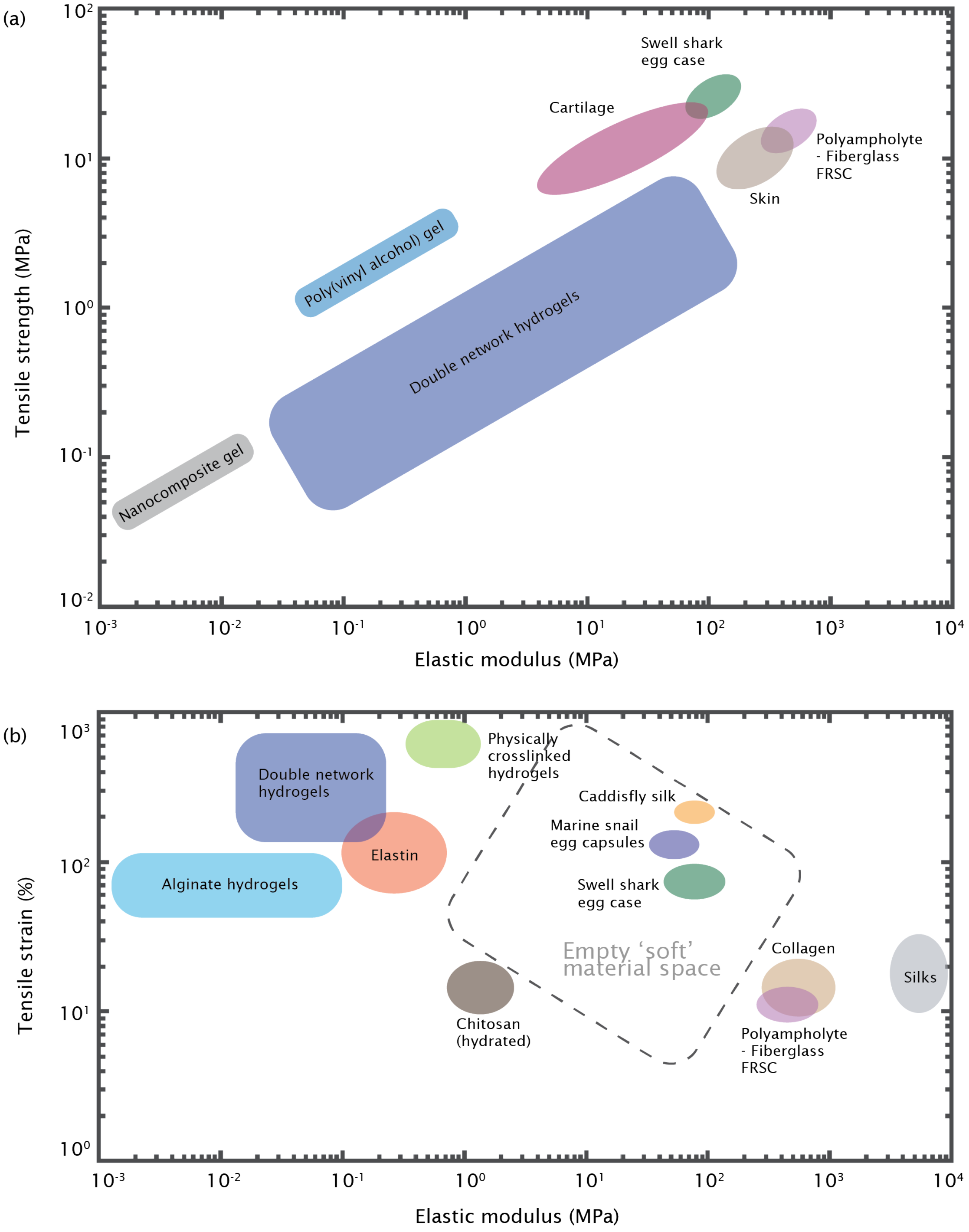

Fig. A2. Ashby plots for soft materials. (a) Tensile strength-Modulus and (b) Tensile strain-Modulus adapted from Li et al.[32], Miserez et al.[33], and King et al.[6]. Boundaries of each material types are approximated. The dotted boundary defines the empty 'soft' material space with intermediary stiffness between stiff and strong with limited extensibility, and soft with high extensibility.

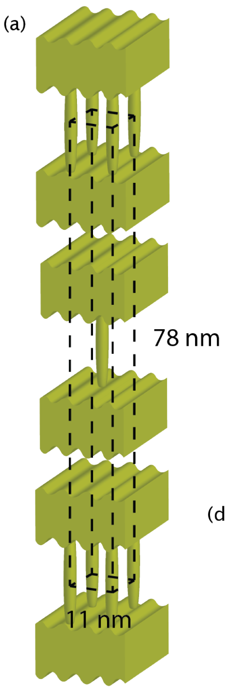

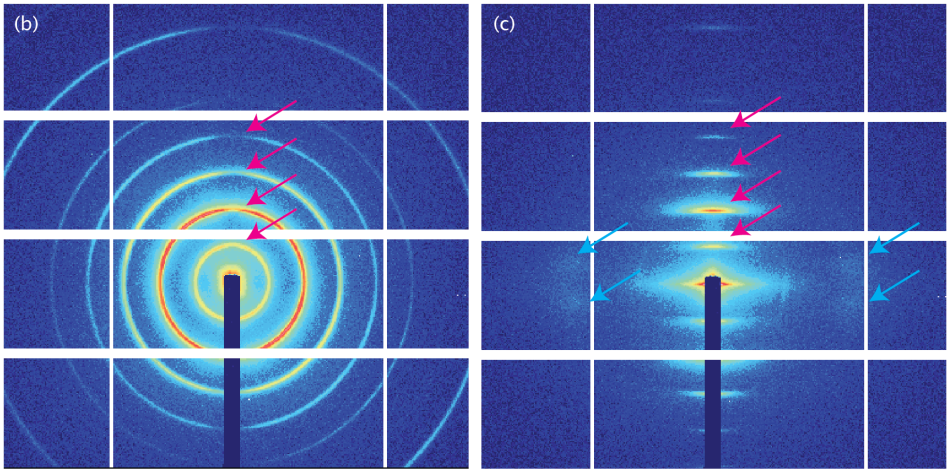

(d)

Lamellar phase scattering peak assignment	BCT phase scattering peak assignment
q*	(002)
2q*	(004)
3q*	(006)
4q*	(008)

Fig. A3. Evidence of a body-centered tetragonal (BCT) nanostructure within the swell shark eggcase. (a) Illustration of body-centered tetragonal (BCT) lattice. (b) Through-plane and (c) on-edge SAXS pattern. Magenta arrows are peaks arising from (00L) scattering, and blue arrows are peaks arising from {101} planes. (d) Lamellar and BCT phase scattering peak assignment.

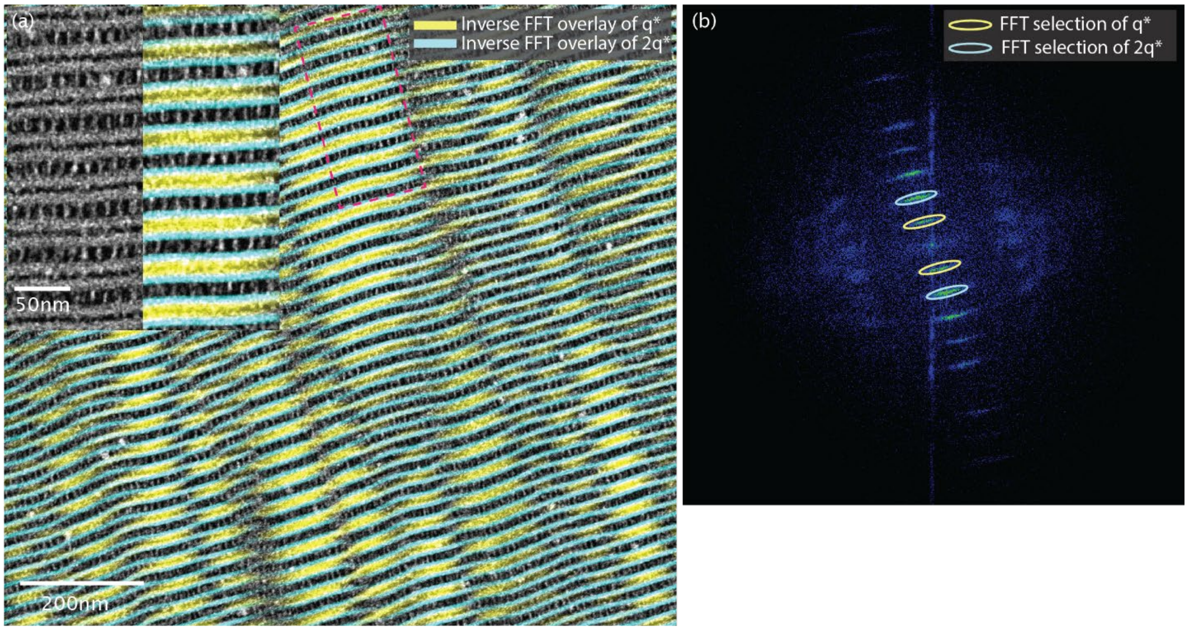

Fig. A4. Inverse FFT overlay of the unstrained swell shark eggcase TEM image. (a) Composite image with the inverse FFT of q* (yellow) and 2q* (cyan) peaks. (b) FFT of the original micrograph illustrating the selected q* and 2q* peaks.

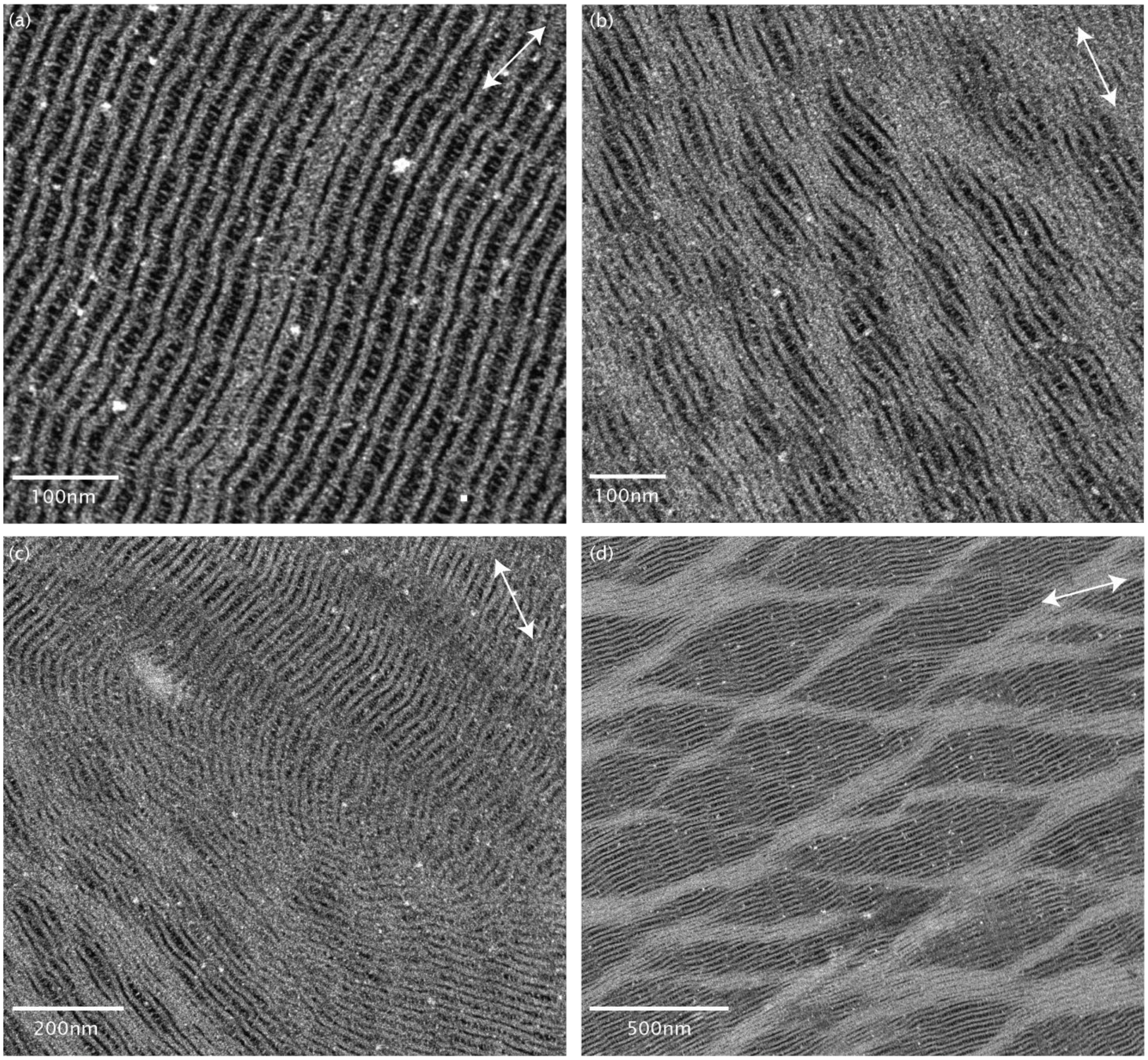

Fig. A5. TEM images of strained eggcases. (a) ~5% strained sample showing onset of shear bands, and 25% strained samples showing (b) nucleation of shear bands, (c) rotation of lattice and (d) diamond-shaped damage zones arising from shear bands. Arrows represent the stress axis.

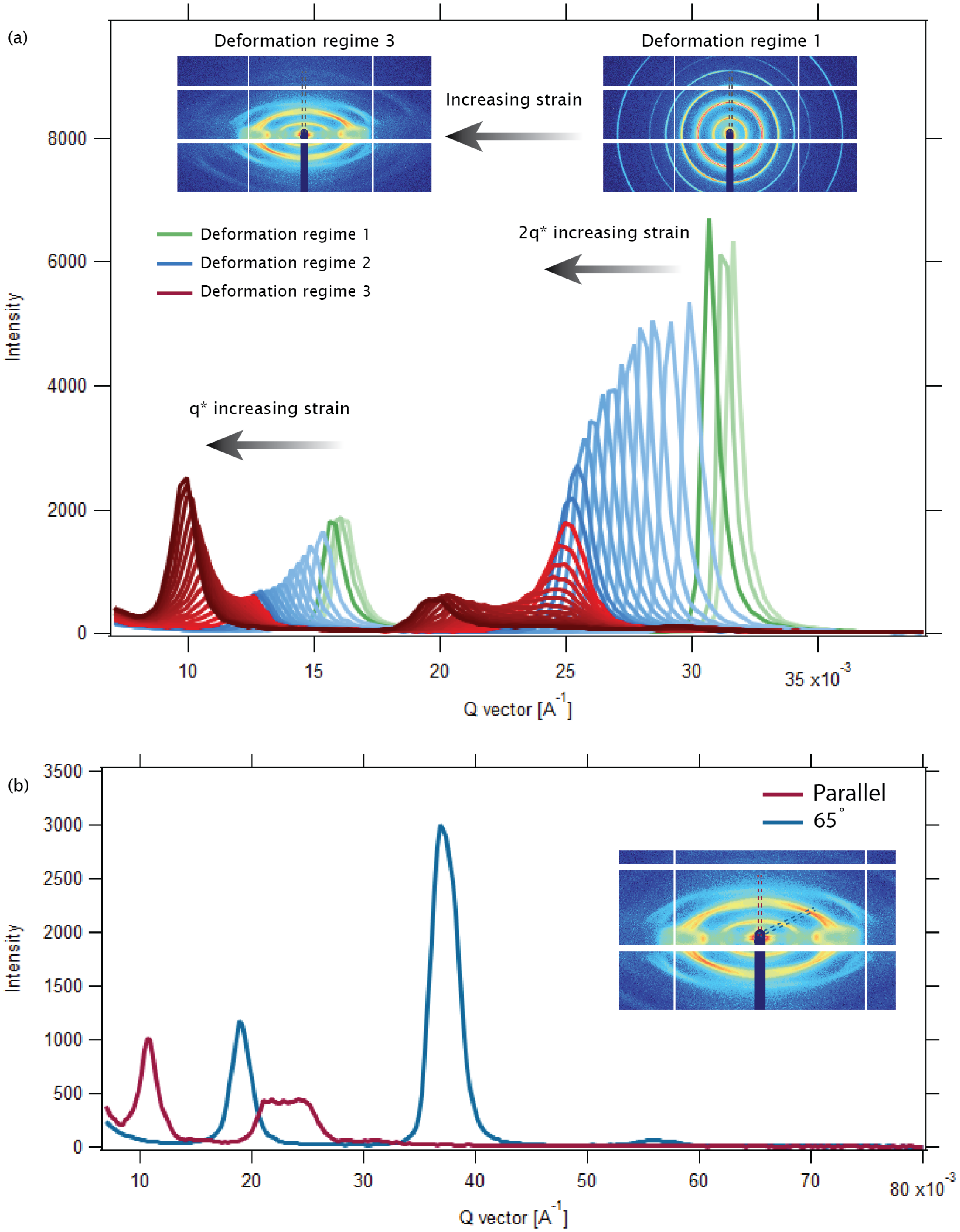

Fig. A6. Disruption of superlattice symmetry as seen in SAXS at DR3. (a) Integrated intensity of SAXS pattern parallel to the stress axis during sample deformation. Color represents the deformation regime and darker shade represents increasing strain. (b) Integrated intensity of SAXS pattern parallel and 65˚ with respect to the stress axis at 50% strain. Insets illustrate angle of integrated lines with respect to 2D SAXS patterns.

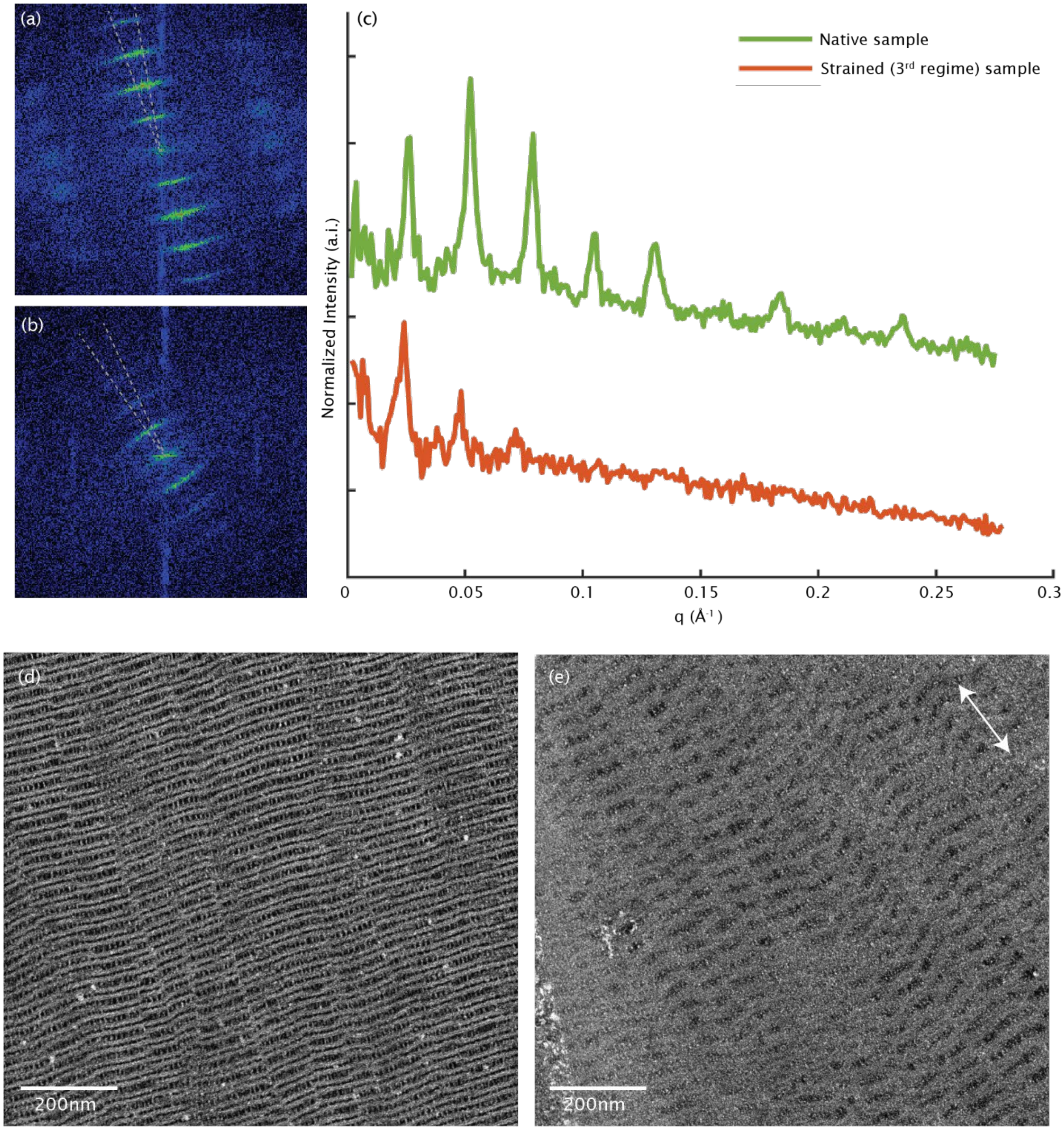

Fig. A7. TEM analyses of eggcase strained to DR3. FFT of (a) unstrained sample and (b) 54% strained sample. (c) Integrated intensity along q* peaks. Corresponding TEM micrographs of (d) unstrained sample and (e) 54% strained sample. Arrow represents the stress axis.

2.6 ACKNOWLEDGMENTS

This work was done in collaboration with Scott P.O. Danielsen, Eric Schaible, Robert M. McMeeking, J. Herbert Waite.

We thank R. Segalman, M. Valentine, A. Kossa, Y. Li, A. Miserez, A. Patterson, J. Booth, K.S. Qwah, and B. Tan for the productive discussions, C. Pierre, C. Orsini and S. Simon from UCSB Marine Operations and The REEF for the collection and generous contribution of the eggcases, and A. Taylor for his technical assistance. The research reported here was supported in part by the National Science Foundation (NSF) Materials Research Science and Engineering Center (MRSEC) at UC Santa Barbara (NSF DMR 1720256) through IRG-3. Individual fellowship support of R.G. was provided by Agency for Science, Technology and Research (A*STAR). X-ray scattering was performed at the Advanced Light Source, a DOE Office of Science User Facility (DE-AC02-05CH11231; beamline 7.3.3). We acknowledge the use of the shared facilities of the NSF MRSEC (DMR 1720256), the NRI-MCDB Microscopy Facility, and the research facilities within California NanoSystems Institute, supported by UC Santa Barbara, and the UC Office of the President at UC, Santa Barbara.

2.7 REFERENCES

1. Chang, Y. & Chen, P.-Y. Hierarchical structure and mechanical properties of snake (Naja atra) and turtle (Ocadia sinensis) eggshells. *Acta Biomater.* **31**, 33–49 (2016).
2. Hahn, E. N. *et al.* Nature's technical ceramic: the avian eggshell. *J. R. Soc. Interface* **14**, 20160804 (2017).
3. Miserez, A., Wasko, S. S., Carpenter, C. F. & Waite, J. H. Non-entropic and reversible long-range deformation of an encapsulating bioelastomer. *Nat. Mater.* **8**, 910–916 (2009).
4. Knight, D. P., Feng, D. & Stewart, M. Structure and Function of the Salachian Egg Case. *Biol. Rev.* **71**, 81–111 (1996).
5. Knight, D. P. & Hunt, S. Fibril structure of collagen in egg capsule of dogfish. *Nature* **249**, 379–380 (1974).
6. King, D. R. *et al.* Extremely tough composites from fabric reinforced polyampholyte hydrogels. *Mater. Horiz.* **2**, 584–591 (2015).
7. Yan, L., Li, Y. S., Xiang, C. B. & Xianda, S. Effect of nano-sized Al2O3-particle addition on PVDF ultrafiltration membrane performance. *J. Membr. Sci.* **276**, 162–167 (2006).
8. Landsman, M. R. *et al.* Water Treatment: Are Membranes the Panacea? *Annu. Rev. Chem. Biomol. Eng.* **11**, 559–585 (2020).
9. Bauer, J. *et al.* Nanolattices: An Emerging Class of Mechanical Metamaterials. *Adv. Mater.* **29**, 1701850 (2017).
10. Denny, M. *Biology and the Mechanics of the Wave-Swept Environment*. *Biology and the Mechanics of the Wave-Swept Environment* (Princeton University Press, 2014).
11. Chen, Q., Chen, H., Zhu, L. & Zheng, J. Fundamentals of double network hydrogels. *J. Mater. Chem. B* **3**, 3654–3676 (2015).
12. Zimmermann, E. A. *et al.* Mechanical adaptability of the Bouligand-type structure in natural dermal armour. *Nat. Commun.* **4**, 2634 (2013).
13. Quan, H., Yang, W., Schaible, E., Ritchie, R. O. & Meyers, M. A. Novel Defense Mechanisms in the Armor of the Scales of the "Living Fossil" Coelacanth Fish. *Adv. Funct. Mater.* **28**, 1804237 (2018).
14. Crosby, A. J. & Lee, J.-Y. Polymer Nanocomposites: The "Nano" Effect on Mechanical Properties. *Polym. Rev.* **47**, 217–229 (2007).
15. Knupp, C., Chew, M., Morris, E. & Squire, J. Three-Dimensional Reconstruction of a Collagen IV Analogue in the Dogfish Egg Case Wall. *J. Struct. Biol.* **117**, 209–221 (1996).
16. Shim, J., Bates, F. S. & Lodge, T. P. Superlattice by charged block copolymer self-assembly. *Nat. Commun.* **10**, 2108 (2019).
17. Jeen, H. *et al.* Reversible redox reactions in an epitaxially stabilized SrCoOx oxygen sponge. *Nat. Mater.* **12**, 1057–1063 (2013).
18. Fratzl, P. *et al.* Fibrillar Structure and Mechanical Properties of Collagen. *J. Struct. Biol.* **122**, 119–122 (1998).
19. Nizolek, T. J., Pollock, T. M. & McMeeking, R. M. Kink band and shear band localization in anisotropic perfectly plastic solids. *J. Mech. Phys. Solids* **146**, 104183 (2021).

20. Albe, K., Ritter, Y. & Şopu, D. Enhancing the plasticity of metallic glasses: Shear band formation, nanocomposites and nanoglasses investigated by molecular dynamics simulations. *Mech. Mater.* **67**, 94–103 (2013).
21. Sasaki, N. & Odajima, S. Elongation mechanism of collagen fibrils and force-strain relations of tendon at each level of structural hierarchy. *J. Biomech.* **29**, 1131–1136 (1996).
22. Notario, B., Pinto, J. & Rodriguez-Perez, M. A. Nanoporous polymeric materials: A new class of materials with enhanced properties. *Prog. Mater. Sci.* **78–79**, 93–139 (2016).
23. Bauer, J., Schroer, A., Schwaiger, R. & Kraft, O. Approaching theoretical strength in glassy carbon nanolattices. *Nat. Mater.* **15**, 438–443 (2016).
24. Zhao, X. Designing toughness and strength for soft materials. *Proc. Natl. Acad. Sci.* **114**, 8138–8140 (2017).
25. Gao, H., Ji, B., Jager, I. L., Arzt, E. & Fratzl, P. Materials become insensitive to flaws at nanoscale: Lessons from nature. *Proc. Natl. Acad. Sci.* **100**, 5597–5600 (2003).
26. Ritchie, R. O. The conflicts between strength and toughness. *Nat. Mater.* **10**, 817–822 (2011).
27. Brown, C. L. & Craig, S. L. Molecular engineering of mechanophore activity for stress-responsive polymeric materials. *Chem. Sci.* **6**, 2158–2165 (1393).
28. Montanaro, J., Gruber, D. & Leisch, N. Improved ultrastructure of marine invertebrates using non-toxic buffers. *PeerJ* **4**, e1860 (2016).
29. Hexemer, A. *et al.* A SAXS/WAXS/GISAXS Beamline with Multilayer Monochromator. *J. Phys. Conf. Ser.* **247**, 012007 (2010).
30. Ilavsky, J. Nika: software for two-dimensional data reduction. *J. Appl. Crystallogr.* **45**, 324–328 (2012).
31. Hill, R. *The Mathematical Theory of Plasticity*. (Oxford University Press, 1950).
32. Li, J., Suo, Z. & J. Vlassak, J. Stiff, strong, and tough hydrogels with good chemical stability. *J. Mater. Chem. B* **2**, 6708–6713 (2014).
33. Miserez, A., Weaver, J. C. & Chaudhuri, O. Biological materials and molecular biomimetics – filling up the empty soft materials space for tissue engineering applications. *J. Mater. Chem. B* **3**, 13–24 (2015).

3 NANOLATTICE-FORMING HYBRID COLLAGENS IN PROTECTIVE SHARK EGGCASES

The permeable protective eggcase of elasmobranchs rely on its hierarchically ordered nanoarchitecture for its properties: distinctive features of its protein self-organization. Although the eggcase precursors are known to undergo intermediate liquid crystalline phase transitions before being structurally arrested in the final nanolattice architecture, the enabling molecular sequence remains a challenge to characterize due to its highly crosslinked nature. By leveraging RNA-seq and proteomic techniques, we identified a cohort of eggcase-forming proteins comprising a collagenous midblock flanked by domains typically associated with the complement of innate immunity and network-forming collagens, type VIII and X. Structurally homologous proteins were found in the genomes of other eggcase-producing cartilaginous fishes, suggesting a conserved molecular self-assembly strategy. The identity and stabilizing role of thiol-derived crosslinks were subsequently elucidated using LC-MS/MS and *in-situ* small angle X-ray scattering. These discoveries provide a new paradigm for the self-assembly of structural metamaterials, protein-based liquid crystalline elastomers, and well-defined porous membranes.

3.1 INTRODUCTION

The survival of all living organisms depends on the presence and functional properties of passive protective structures. Passive structures such as skin provide effective barriers against episodic environmental insults such as infectious agents, corrosives, foulants, and predators and are multifunctional with critical roles in maintaining heat and water balance[1]; in fertilized eggs, eggshells[2] and eggcases[3,4] ensure insulation and metabolic/respiratory waste exchange. Shark and skate egg cases, with their exquisite textures and shapes, have long been objects of fascination as their sobriquet 'mermaid's purses' attests. Recent breakthroughs on the swell shark eggcase have shown that this fascination is not undeserved – the eggcase features excellent mechanical properties, selective permeability, and an intricate hierarchical architecture ranging from centimeters down to the nanometer lengthscale[3]. Eggcase architecture is comprised of nanoribbons assembled in Bouligand-like twists resembling synthetic fiber-reinforced composites. However, a distinguishing factor is the nanolattice — a mechanical metamaterial — that constitutes these nanoribbons. The nanolattice provides lattice-governed plasticity mechanisms that include uniform nucleation of nanoscale shear bands, and orientation-dependent lattice rotation that facilitates shear band formation[3]. The unique architecture enables the multifunctional eggcase to achieve a tactical balance between two opposing attributes that are mandatory for survival — porosity and mechanical toughness (Fig. 3.1).

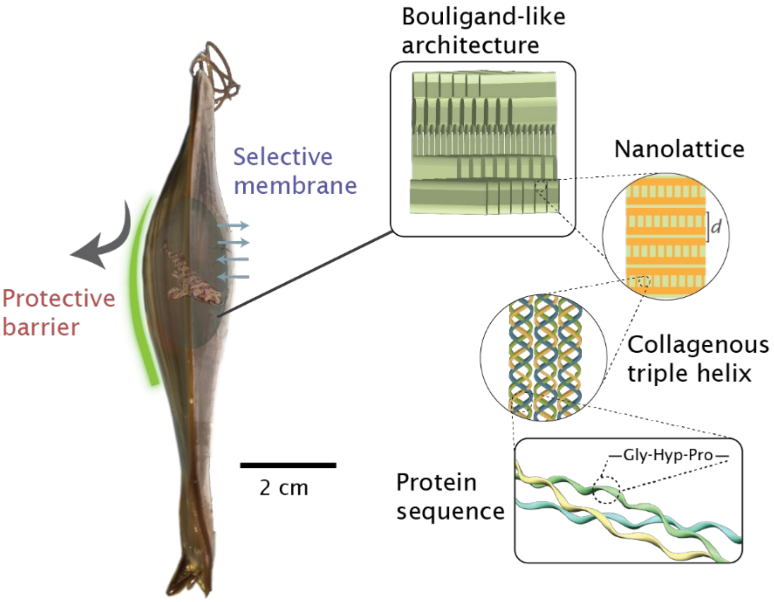

Fig 3.1. Illustration of the multifunctionality and hierarchical organization of the collagenous eggcase. The eggcase of swell sharks provides the delicate developing embryos with a tough barrier against environmental threats as well as being a selective membrane against infectious agents while allowing gaseous and metabolic waste exchange. The periodic 39 nm *d-spacing* in the nanolattice has been previous characterized using SAXS and electron microscopy[3].

Earlier studies on the formation of elasmobranch eggcases elucidated multiple intermediate lyotropic liquid crystalline phases that exist in storage granules of the eggcase-producing nidamental gland. The lyotropic phases include micellar, lamellar, cholesteric, hexagonal, and a phase equivalent to the nanolattice seen in the final eggcase[5]. These transitions are proposed to be influenced by both pH and concentration[6]. The eventual structure is then further stabilized via oxidative covalent crosslinking[4] which results in a highly ordered, anisotropic, and arrested nanoarchitecture that is comparatively analogous to synthetic liquid crystalline elastomers[7]. As with proteinaceous materials, the basis of the architecture is revealed by the primary protein sequence (Fig. 3.1). Our aim here is to identify the eggcase proteins behind the self-assembly of the nanolattice as well as to distill the molecular design principles for future inspirations in the development of materials where both strength and well-defined selective permeability are desirable.

Structural proteins have been notoriously challenging to sequence due to their tanned highly crosslinked nature and the consequent insolubility. In this work, we leveraged RNA-sequencing and proteomic techniques[8] to obtain the complete sequence of the eggcase-forming protein and identify crosslinks involved in mechanical and structural reinforcement. This newly identified cohort of proteins is distinguished by a contiguous modular series of collagens flanked by short consensus repeats (SCR) and C1q globular (gC1q) domains — two protein domains that are classically associated with proteins of the immune system[9,10]. A database search based on our results revealed proteins with similar structural configurations in the genomes of both oviparous and ovoviviparous elasmobranchs and chimaera — suggesting a conserved molecular strategy for the assembly of eggcases of cartilaginous fishes. Using amino acid analysis and liquid chromatography coupled with tandem mass spectrometry (LC-MS/MS) of eggcase hydrolysates, along with *in-situ* small angle X-ray scattering (SAXS) during tensile deformation, we identified chemical crosslinks within the eggcase and elucidated the structural and mechanical role of thiol-derived crosslinks. The results of this work advance the understanding of the distinctive network-forming collagens and foster the development of supramolecular nanoarchitectonics[11]. The strategies seen in the eggcase provide a new paradigm for the self-assembly of mechanical metamaterials[12], liquid crystalline elastomers[13], and ultrafiltration[14] and immunoisolation membranes where well-defined pore sizes are sought-after[15,16].

3.2 RESULTS

C. ventriosum collagenous eggcase-forming proteins

The existence of triple-helical collagens in elasmobranch eggcases was established previously by X-ray scattering, amino acid composition, and thermal shrinkage studies[4]. However, efforts to characterize these eggcase-forming proteins from the gland extracts of a related elasmobranch (dogfish) by Edman sequencing yielded only limited protein sequences[17]. To further investigate the full-length sequence of the collagenous eggcase protein, we established a transcriptome library from mRNA isolated from the nidamental gland of a gravid swell shark, an elasmobranch endemic to the coast of central California. The library was assembled by *de novo* transcript assembly of short reads using the Trinity software suite[18].

Owing to native collagen's resistance to pepsin[19], we narrowed the search for collagenous eggcase-forming proteins by pepsinization of the eggcase followed by in-gel tryptic digestion. To identify the collagenous proteins and their post-translational modifications, the digested peptides were characterized with LC-MS/MS and the results were *de novo* assembled and searched against virtual sequences predicted from the open-reading frames of the transcriptome library.

Eggcase-forming proteins, purseins, were identified and are distinguished by a contiguous series of SCR, collagen, and gC1q domains. To simplify, we retain the nomenclature of collagens and refer to the non-collagenous C-terminal domain and N-terminal domain(s) as NC1 and NC2 (Fig. 3.2). Variants pursein-1 and pursein-2 differ by the number of the SCRs. In all cases, an acidic patch with an isoelectric point of ~4 and a signal peptide were observed at the N-terminal of the virtual sequences but were not detected by LC-MS/MS. On the other hand, partial coverage of the NC2 domain in pursein-1b and NC1 domains in all three purseins suggests that these domains were not proteolytically processed in the final assembly of the eggcase (Fig. B1). Alignment of the pursein sequences showed similarities between the sparse partial sequences of the NC2 and collagenous domains of the dogfish eggcase proteins[17].

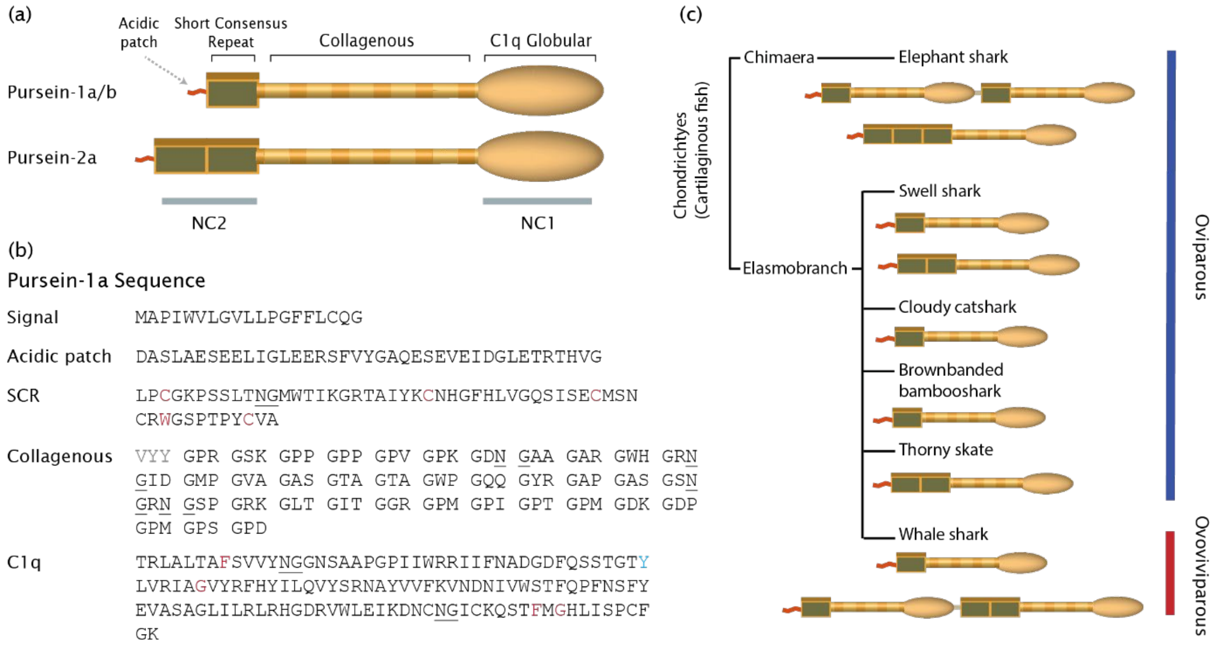

Fig. 3.2. (a) Illustration of purseins showing structural homology and the contiguity of the domains. (b) Sequence of pursein-1a with consensus sequences of the domains in red, deviation from gC1q consensus sequence, F → Y^{272}, is in blue. Intermittent sequences are in gray and Asp-Gly pairs are underlined. (c) Structurally homologous sequences found in the annotated genomes of other oviparous and ovoviviparous cartilaginous fishes.

Variable hydroxylation of prolines, deamidation of asparagines, and oxidation of methionine and tryptophan were also predicted from the *de novo* assembled peptide sequences (Fig. B1). At least five incidences of the Asp-Gly dipeptide which is susceptible to spontaneous deamidation[20,21] were seen in all purseins (Fig. 3.2 and B1) and correlate well with the locations of the variably deamidated asparagines. Analysis of the collagenous region of the pursein sequences also indicated the unusual presence of helix destabilizing aromatic residues – tryptophan and tyrosines[22]. By contrast, cysteines were observed to be localized to the non-collagenous flanking domains.

While the tandem configuration of the three modules is unique to purseins, the collagen-gC1q configuration is also seen in C1q proteins and network-forming collagens, type VIII and X[23]. Multi-sequence alignment of gC1q modules indicated the conservation of key hydrophobic core residues except for a F → Y^{272} substitution in pursein-1a[23]. Alignment of the SCR domains confirmed the conservation of the consensus sequence which includes four invariant cysteines and one tryptophan, and other mostly invariant prolines, glycines, and hydrophobic residues (Fig. 3.2 and B2)[10]. These invariant cysteines are known to form specific intradomain disulfide bonds having a 1 – 3 and 2 – 4 configuration.

Conserved molecular strategy of eggcase-forming proteins

Protein sequences of purseins were searched against the non-redundant protein database on NCBI using the BLAST algorithm[24]. Proteins with similar configurations were identified in both oviparous and ovoviviparous, elasmobranchs and chimaera (Fig. 3.2). Extensive scans of the other similar proteins originating from species not belonging in either of these classifications do not share the same structural configurations that are unique to purseins. In all cases of proteins identified through the search, the proteins were made of varied configurations of the same three modules that were observed in purseins. These proteins were designated as uncharacterized or vaguely classified based on similarities with known proteins such as collagen and C1q. Collagenous domains in these proteins were similar in length, ~118 amino acids. Comparatively, the triple-helical domains of collagen type VIII and X are ~456 residues, and ~78 residues long for C1q proteins (Fig. B3).

Signal peptides were identified in all pursein-like proteins except for the proteins identified in the whale shark genome. It is important to note that the whale shark is the largest aquatic non-mammal and the only ovoviviparous elasmobranch under comparison[25]. The lack of signal peptide may suggest a different mode of secretion, e.g. by holocrine secretion as in the secretion of hagfish slime, involving the rupture of the cellular plasma membrane[26].

Amino acid analysis and crosslink identification

The amino acid compositions of eggcase hydrolysates closely resembles the composition profile of the purseins. The presence of ~17% Gly and ~9% Pro and ~2% hydroxyproline (Hyp) agrees with the collagenous nature of purseins (Table B1). ~0.4% dihydroxyphenylalanine (DOPA) were also detected. Cysteines were protected during hydrolysis by alkylation with iodoacetamide and ~0.23% of cysteines were observed in the native samples. Comparison with the hydrolysate composition of DTT-reduced eggcase indicated that ~0.83% cysteines were present as solvent-accessible crosslinks and could be reduced by DTT. Discrepancies between the hydrolysate composition and the virtual sequence could potentially arise from differences in the ratio of purseins, unaccounted tryptophans which are unstable during hydrolysis by hydrochloric acid, as well as contributions potentially from a matrix protein that has yet to be characterized.

Empirical evidence of a change in eggcase color from dark-green to orange-green upon treatment with 10 mM DTT suggests the presence of reducible aromatic cross-links besides cystines. Given the involvement of DOPA in the eggcase tanning process[4], the eggcase was hydrolyzed for 2 hours and passed through a phenylboronate affinity column to isolate possible cis-diols (e.g. catecholic compounds). Isolated compounds were subsequently characterized with LC-MS. Masses corresponding to DOPA and cysteinyl-DOPA were detected with LC-MS. The identity of cysteinyl-DOPA was further confirmed by its LC-MS/MS fragmentation mass spectrum (Fig. B4)[27,28]. A mass corresponding to histidyl-DOPA was observed in LC-MS but awaits confirmation by LC-MS/MS (Table B2).

Mechanical and structural role of reducible cross-links

Results in the preceding sections suggest that the intermediate lyotropic liquid crystalline phase reported in earlier studies[6,7] is formed by collagenous proteins with flanking domains stabilized by at least two different cysteinyl-derived crosslinks: disulfides and cysteinyl-Dopa or Dopaquinones. Both are reducible, but the disulfide is more cleavable by reduction than Cys-Dopa. If DTT treatment cleaves disulfides but only bleaches Cys-Dopa/quinones without cleavage, then we expect DTT to render eggcase softer and more extensible. To further elucidate the mechanical and structural role of crosslinks that are localized in the non-collagenous domains, eggcases were subjected to chemical reduction with DTT for 24 hours and characterized with *in-situ* SAXS during tensile testing.

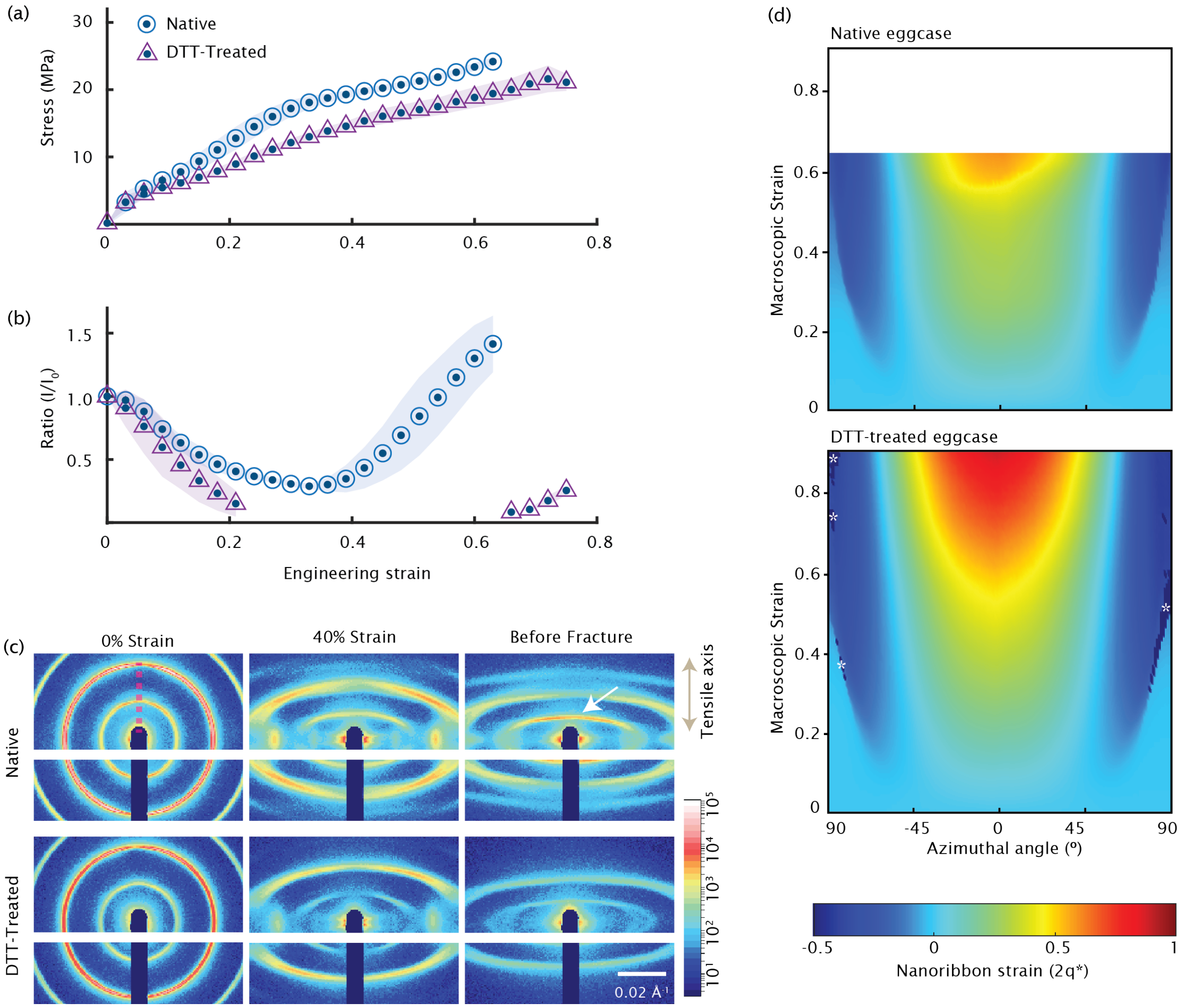

Fig. 3.3. (a) Stress-strain curve of native and DTT-treated eggcase strained along the long-axis of the eggcase and measured with *in-situ* SAXS during tensile deformation. (b) Intensity of q* plotted against strain for the corresponding samples. (c) 2D-SAXS of samples at various strains. Arrow (white) highlights the increase in q* intensity along the stress axis seen in the native sample at the 3rd deformation regime. (d) Angular distribution of nanoribbon strain for native and DTT-treated eggcase derived from determining 2q* across 0 — 180˚, where 0˚ indicates the stress axis. Dark blue regions marked with an asterisk are areas where signal intensity is too low for quantification of strain.

Treatment with DTT resulted in an increase in strain to failure from 0.659 ± 0.03 to 0.821 ± 0.09 with a general decrease in the strain hardening observed in the 2nd and 3rd deformation regime[3]. Changes to the initial modulus were minimal and within standard deviation (Fig. 3.3a). The 39 nm periodic *d*-spacing of the nanoribbons arising from the constituting nanolattices gives rise to the observed q* and the corresponding higher-order reflections. Therefore, analyses of the peak intensities and peak positions would inform us on the relative disorder and strain of the nanolattice[3]. Despite the minimal differences in the initial modulus, analyzing the primary q* peaks parallel to the stress axis revealed a higher rate of nanolattice disordering. This was indicated by a steeper decrease in peak intensity in the DTT-treated samples and the complete disappearance of the peak between 20% – 60% strain of the 2nd and 3rd regimes (Fig. 3.3b).

In the native sample, a remarkable strain alignment is seen parallel to the stress axis at the 3rd deformation regime[3]. This phenomenon was less pronounced in the DTT-treated sample (Fig. 3.3b and c) and demonstrated the importance of the crosslinks for maintaining nanolattice structural integrity against deformation and for facilitating strain alignment.

Analyzing the strains by comparing the changes in 2q* during strain indicate a higher strain to failure of DTT-treated nanoribbons that are parallel to the stress axis. The results of the DTT-treated samples agree with our previous assessment where the nanoribbon strain correlates to the macroscopic strain, indicating minimal matrix strain in this orientation. This is contrary to observations of deformation on collagen in tendon and fish scales.

Observations of the nanoribbon strain distribution indicates a clear delineation between elongation and contraction of nanoribbons at ~±50˚, where nanoribbons along the boundary have ~0 strain (Fig. 3.3d). As the angle of ~50˚ closely corresponds to the orientation with the highest amount of shear (45˚), shear-dominant deformation mechanisms such as fibril sliding might be the primary strain mechanism, which results in no changes of *d-spacings*. The roughly consistent strain distribution and elongation-contraction delineation between the native and DTT-treated samples imply that these mechanisms were not influenced by the chemical reduction of the eggcase. Since a 'softening' of the matrix would promote fibril sliding that results in lower nanoribbon strains within the eggcase, the consistent results suggest that the matrix is not strongly influenced by DTT-treatment. Further identification and investigation of the interfibrillar matrix is required to ascertain this conclusion.

3.3 DISCUSSION

Survival of embryos of oviparous sharks depends on the tough yet permeable material that encases and protects the embryos from the environment. This dual functionality can be attributed to the intricate hierarchical structure and the nanolattice architecture of the eggcase. Key to the nanolattice self-assembly is the molecular structure of the pursein building blocks that enable a liquid crystalline assembly leading to the permeable nanolattice[5–7]. This study provides the first glimpse of a biological strategy in which formation of a multifunctional membrane is mediated by macromolecular liquid crystals.

Our most noteworthy breakthrough is the discovery of a new class of modular eggcase-forming proteins that are made up of SCR, collagen, and gC1q domains. Structurally homologous proteins were identified from the published genomes of other oviparous and ovoviviparous cartilaginous fish, suggesting a conserved strategy among elasmobranchs and chimaeras. Intriguingly, both NC1 and NC2 of purseins are composed of domains that are crucial components of the complement system on which innate immunity depends. In the complement system, complement receptor type 1 (CR1), a protein consisting of 30 tandem SCRs, binds to C1q proteins via its collagen stalk and gC1q domain[29,30] – suggesting probable telechelic interactions between the flanking domains of purseins.

Owing to its propensity to trimerize, gC1q in collagen type X has also been demonstrated to be an important trimerization domain with the ability to form hexamers[31] . Since collagens are prone to misfolding due to the ease of misalignment of the repetitive $(GXY)_n$ motifs, terminal trimerization domains ensures lateral register that is necessary during folding of the collagen triple helix. This improves the stability of the collagen and enables proper refolding[32]. Besides, the exposed strips of hydrophobic aromatic residues seen in the gC1q domains of collagen type VIII and X have been previously proposed to drive higher-order supramolecular assembly leading to the non-stochastic tetrahedral and hexagonal networks[33,34]. Homology models of the NC1 domains of purseins elucidated an intriguing aromatic 'crown' on the surface (Fig. B3), suggesting that a similar phenomenon as proposed in type VIII and X collagen might facilitate the supramolecular assembly of the nanolattice architecture. Intriguingly, arginines were observed in the vicinity of these aromatic residues across all purseins, hinting at the possibility of π-cation contributions to the self-assembly process[35]. Protein hydropathy analysis indicates a consistent pattern of hydrophilic domain flanked by comparatively more hydrophobic domains in purseins — resembling amphiphilic lyotropic mesogens (Fig. B5)[7,36]. Hence, along with possible π-cation and SCR-collagen-gC1q interactions, hydrophobic interactions may be part of the process that drives the supramolecular formation of a lyotropic lamellar phase bridged by collagenous struts.

The terminal modules of purseins are further reinforced by cysteinyl-crosslinks, that when chemically reduced, result in eggcase softening and increased nanolattice disordering. Consistent with this is a decrease in resistance of the DTT-treated terminal modules towards pepsinization. Since pepsin resistance of these domains is due to occlusion of vulnerable sites in the native structure, the decrease in resistance emphasizes the necessity of thiol-derived-crosslinks for maintaining the tightly folded terminal secondary structures. These results agree with the observations of the highly conserved cysteines within NC2 forming intra-molecular crosslinks[10]. Furthermore, this also indicates that cysteines of NC1 form inter- or intramolecular crosslinking despite not sharing the same conserved cysteine positions as C1q proteins[9].

To estimate the length of purseins, we assumed a collagenous triple helix with a rise per residue of ~0.29 nm[37,38] which would result in a collagen length of ~34 nm. The gC1q trimer of collagen type X has a structure that is similar to a truncated cone that is ~5 nm in diameter[23,33], while a single SCR module of CR1 has an averaged native length of ~2.9 nm[10].

Summing these distances coincides with the expected length of proteins that could give rise to the 39 nm periodicities in the eggcase[3]. Indeed, these dimensions are in rough agreement with transmission electron microscopy (TEM) observations of the purified dogfish eggcase protein after low-angle unidirectional shadowing[4]. Despite using the term 'gap' to describe regions of lower electron density in the nanolattice, we believe that the absence of a regular structure under TEM is a limitation of our staining methods leading to the lack of resolution of finer structures in the gap. A similar argument has been made in the dogfish eggcase and was subsequently proven using metal-shadowed replicas that provided higher resolution of the architecture[39]. Based on unit cell symmetry observations, a model involving axially staggered molecules with interacting globular domains was proposed for the dogfish eggcase[39]. The protomers are assembled into octamers with four protomers axially shifted by ~15 nm with respect to the other four. Building onto the proposed model for the dogfish eggcase with knowledge of specific sequence — we propose that these staggered pairs of four protomers can align either in a parallel or antiparallel fashion to form the octamers, while the terminal domains facilitate the self-assembly by serving as both physical and chemical (thiol) crosslinkers. Tying up with the TEM observations[3], the gap region would correspond to the non-overlapping region comprising four protomers, while each strut corresponds to an overlapping region composed of eight protomers (Fig. 3.4).

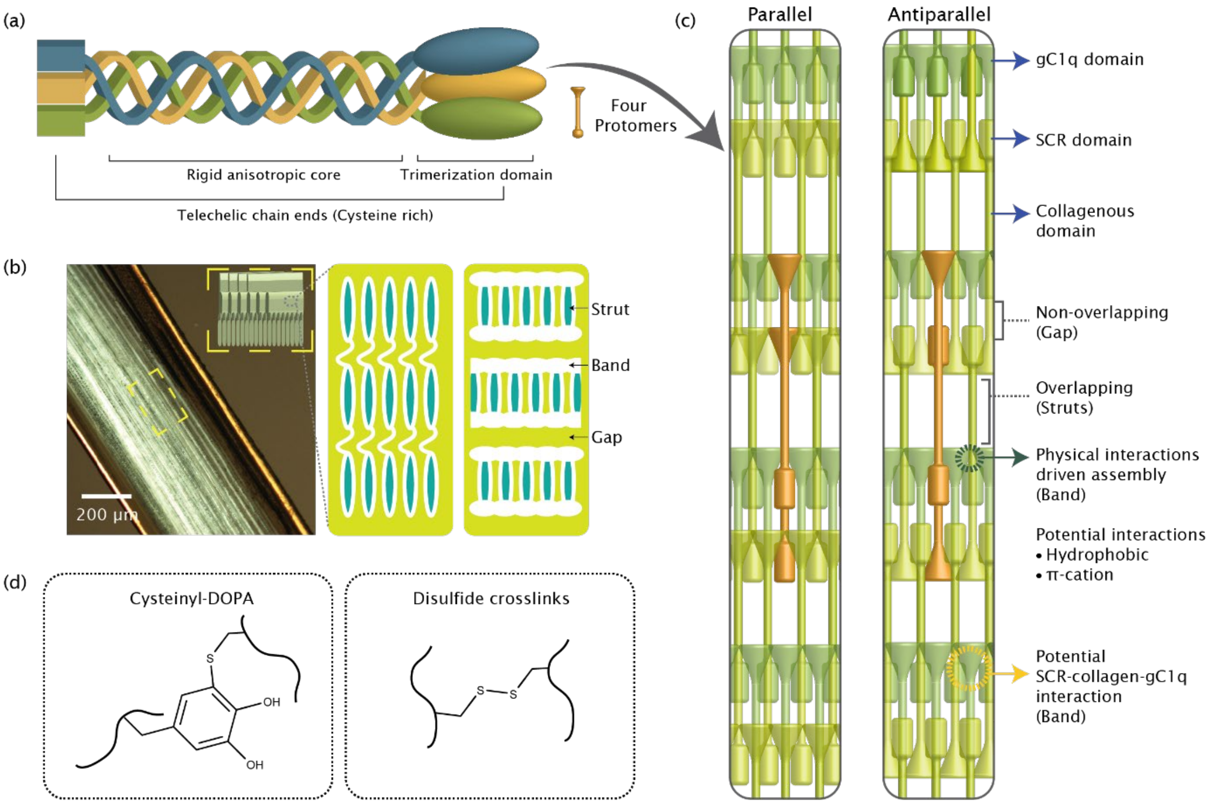

Fig. 3.4. (a) Illustration of a pursein protomer and the functional aspect of each domain in the self-assembly of the nanolattice. (b) Birefringence of the eggcase indicative of molecular anisotropy. Illustrations highlighting the resemblance of a synthetic main chain smectic liquid crystalline elastomer and the nanolattice architecture that is found within the nanoribbons. (c) 2D simplified model of possible molecular arrangements that would result in the nanolattice architecture. (d) Crosslinks identified within the eggcase.

Evidence of molecular[3], optical (Fig. 3.4), and mechanical anisotropy (Fig. B6) supports the notion that the eggcases are analogous to synthetic liquid crystalline elastomers[7,13,40]. While the possible interactions arising from the terminal non-collagenous domains are critical to molecular assembly, the intermediate liquid crystalline phases seen during assembly[5,6] would be just as crucial in determining the long-range order of the nanolattice. The mesogenic properties of collagens can be attributed to the rigidity and the high aspect ratio of the triple helix[41,42]. The advantage of a macromolecular mesogen is apparent in this case as it determines the dimensions of the nanolattice as well as consequent membrane selectivity. The advantage of lyotropic liquid crystalline phases for self-assembly is two-fold: (1) the formation of well-defined non-stochastic permeable networks and (2) processability of dense possibly shear-thinning fluids[43]. These properties are essential for producing dense structural materials from fluidic precursors stored in granules that need to merge into a congruent phase and solidify only when appropriate.

3.4 CONCLUSION

In summary, the collagenous eggcase-forming protein, pursein, was identified and revealed to be a triblock with a trimeric collagenous midblock flanked by terminal domains having propensities to form supramolecular assemblies. The molecular sequence revealed in this study provides an initial blueprint of the necessary parameters for the liquid crystalline assembly of a multifunctional nanolattice with well-defined pores. In contrast to industrial manufacturing practices, biological materials are restricted to mild aqueous processing conditions and natural building blocks. Therefore, elasmobranch eggcases provide us with valuable lessons in ‘green’ processing, and molecular and nanostructural design for tough and permeable membranes. While it is unclear if the genomic sequences of the whale shark and elephant shark eggcase-forming proteins undergo alternative splicing; it is intriguing to consider the various configurations of the three domains and the possible nanoarchitectures that arise from these proteins. Pursein and its self-assembly strategy offer a timely inspiration for novel assembly routes for structural metamaterials, membranes with well-defined porosities, and liquid crystalline elastomers. At a more fundamental level, purseins provide an ideal comparative system for gC1q-containing network-forming collagens, type VIII and X — providing an opportunity to advance the understanding of the self-assembly process and determining the design variables that govern the hexagonal, tetrahedral, or tetragonal geometry of non-stochastic collagen networks.

3.5 MATERIALS AND METHODS

Eggcases and nidamental gland collection

Nidamental glands and eggcases for protein identification and amino acid analyses were obtained from a gravid female swell shark that was freshly collected from the wild and intended for a parasitology class. The shark was euthanized with an overdose of MS-222 by immersion into sodium bicarbonate buffered MS-222 bath (> 250 mg/L). The nidamental glands were stored in RNAlater and stored in -80˚C until needed. Eggcases for crosslink identification were obtained from tank reared swell sharks, sacrificed within 2 months of being laid and stored at -80˚C until needed. The embryos were carefully removed from the eggcase and euthanized with an overdose of MS-222 by immersion into sodium bicarbonate buffered MS-222 bath (1 g/L). The procurement of eggcases is in accordance with Institutional Animal Care and Use Committee (IACUC) guidelines and reviewed by UCSB IACUC.

Transcriptome library construction

RNA-seq analysis was performed as previously described[8]. The nidamental gland was homogenized at 4˚C and total RNA extracted with Monarch® Total RNA Miniprep kit. Samples were dried in RNAstable® and stored at -20˚C. RNA was then resuspended in diethylpyrocarbonate (DEPC) treated water and poly-A mRNA was enriched with oligo dT beads. Subsequent library preparation was done with NEXTflex® Rapid Directional RNA-Seq Library Prep Kit. Library quality was analyzed with Agilent 2100 Bioanalyzer.

The library was then sequenced on an Illumina HiSeq 4000 and 2 x 151 bp paired-end reads were collected. *De novo* transcript assembly was performed on quality-filtered FASTQ sequences with the Trinity software suite on a computational cluster using standard parameters. Putative coding regions from the assembled transcript sequences were extracted with TransDecoder that is part of the Trinity software suite[18].

Preparation and pepsin digestion of eggcase

Eggcases were dialyzed against MilliQ water thrice, 10 minutes each, prior to further processing. Inner and outer cuticles of the eggcases were peeled off, and the mid-layer which comprises the bulk of the eggcase was homogenized in MilliQ water at 4˚C. The homogenized eggcase was then lyophilized, and stored at -80˚C.

Eggcases were pepsinized at a concentration of 1mg/mL (4M urea, 5% acetic acid) at a 1:50 pepsin (Promega) to substrate ratio for 48 hours at 4˚C. Dithiothreitol (DTT) treated sample was treated in 10 mM DTT prior to pepsinization. Samples were clarified by centrifugation and the soluble fractions were dialyzed twice against 0.1M sodium borate (pH 8.0). Dialyzed samples were centrifuged, and the insoluble fractions were washed once with 0.05M sodium borate (pH 8.0), resuspended in 0.1% acetic acid, and dialyzed thrice against 0.1% acetic acid. Dialyzed samples were lyophilized and resolubilized prior to SDS-PAGE. All steps were performed at 4˚C.

Samples were mixed 1:1 with 2X Laemmli buffer containing 100 mM DTT and heated at 70˚C for 10 minutes. Samples were loaded onto a 12% Bis-Tris gel (Bolt) and run at 110V for 1 hour 30 minutes in MOPS running buffer (Bolt). The gel was rinsed thrice with water, stained with 0.1% Coomassie Brilliant Blue R-250 (Bio-Rad) in 20% methanol, 0.1% acetic acid, destained with 30% methanol followed by water. Protein bands were excised using a sterile scalpel blade, covered with 0.1% acetic acid, and shipped to Bioproximity for tryptic digestion and LC-MSMS (Thermo Q-Exactive HF-X Orbitrap mass spectrometer). Acetic acid and water used were LC-MS grade (Optima).

Protein identification, verification, and analysis

LC-MS/MS results were *de novo* assembled and searched against open-reading frames of the transcriptomic library using PEAKS Studio XPro (Bioinformatics Solutions) with post-translational modifications (PTM) being identified in the process. Results were filtered with a 1% false discovery rate threshold, and a minimum of 5% ion intensity for PTMs.

cDNA library for sequence verification by Sanger sequencing was generated from poly-A enriched mRNA. Poly-A mRNA was enriched from total RNA using NEB Magnetic mRNA isolation kit while cDNA library was prepared with NEBNext® Single Cell/Low Input cDNA Synthesis and Amplification Module. Gene-specific primers were designed using Primer-BLAST[44] for PCR amplification and Sanger sequencing. PCR amplification was performed using Phusion® High-Fidelity DNA Polymerase. Pursein-1a had an incomplete 5' end, therefore sequence of the template-switching oligo from the NEBNext cDNA synthesis kit was used as the forward primer along with pursein-1a reverse_1 primer for PCR amplification. Sequencing reads for pursein-1a forward primer were low in quality, and therefore reverse_2 primer was designed for sequencing of the 5’ end of pursein-1a.

Pursein-1a	Forward	CATTGCAAGCAGTGGTATCAA
	Reverse_1	CATTCCTCACAATGACCTGA
	Reverse_2	CAAATAATTGGCCCAGGAGC
Pursein-1b	Forward	AGAGAGATTCTGAAAGCCTG
	Reverse	TTATCCTCTCAGCTCTCAAC
Pursein-2a	Forward	AAGAGAGATTCTGAAAGCCT
	Reverse	CACGCTGTGATTAAGGAAAT

In-silico analyses

Signal peptides were identified using SignalP 5.0[45]. All signal peptides had a probability of > 98%. However, the exact cleavage site for pursein-1a was ill-defined with the most probable site having a probability of 49.8%. Multiple sequence alignment of proteins was performed on ClustalW[46]. UniProt accession numbers of proteins used in the alignments are P02745, P02746, P02747, P27658, P25067, Q03692, and P17927.

Homologous proteins were searched using BlastP with pursein sequences against the non-redundant protein database. Sequences identified were then scanned using ScanProsite for contiguous SCR, collagenous, and gC1q domains. Signal peptides were identified as before. Signal peptides in the proteins of the cloudy catshark and thorny skate were detected only with start codons further downstream than the one indicated. Accession numbers of the protein sequences are XP_032902287.1, XP_007894850.1, XP_007894575.1, GCC26270.1, XP_020368837.1, XP_020368836.1, and GCB65488.1.

The sequence of gC1q domains in purseins were identified using ScanProsite[47] and submitted to SwissModel[48] for homology modelling. The crystal structure of the homotrimer of collagen X[33] was used as the template for the homology model. GMQE scores were 0.67, 0.69, and 0.61 and QMEAN Z-scores were -3.27, -2.70, and -2.57 for purseins-1a, 1b, and 2a respectively. Regions that are best modelled corresponded to the conserved core β-sandwich scaffold[9]. Results were exported and the protein surface was visualized using ChimeraX (version 1.1)[49].

Hydropathy plots of purseins were obtained with Expasy ProtScale using the hydrophobic scale developed by Miyazawa and Jernigan[50] with a 21-residue window size. Sequence of the signal peptides was not included in the hydropathy plots.

Amino acid hydrolysis and analysis

Homogenized and lyophilized eggcase was treated with 10 mM DTT for 24 hours at 4˚C and treated with 50 mM iodoacetamide in 100 mM ammonium bicarbonate for 40 minutes in the dark. Samples were centrifuged at 14000 X g, the supernatant was removed, and the pellet resuspended in MilliQ water for a total of three times. DTT treatment was omitted to compare the amount of cysteines in the native and the reduced state. Cysteine was detected as carboxymethylcysteine. Samples were then lyophilized and resuspended in 500 µL of 6 M HCl and 5% phenol at ~2 mg/mL, vacuum sealed, and hydrolyzed at 110˚C for 24 hours. The hydrolysates were cleaned up by complete evaporation on a SpeedVac (Savant) followed by resuspension and evaporation, thrice with 200 µL of MilliQ water and thrice with 200 µL of ethanol. Samples were then resuspended in 0.01 N HCl and loaded onto the automated amino acid analyzer (Hitachi High-Technologies L-8900).

Isolation of DOPA-containing crosslinks and identification with LC-MSMS

Homogenized and lyophilized eggcase were resuspended in 6 M HCl and 5% phenol, vacuum sealed, and hydrolyzed at 110˚C for 2 hours. The hydrolysates were cleaned up by complete evaporation on a SpeedVac (Savant) followed by resuspension and evaporation, thrice with 200 µL of MilliQ water and thrice with 200 µL of ethanol. The hydrolysate was then resuspended in 0.1M sodium phosphate buffer (pH 7.4), and centrifuged at 14000 X g, the soluble supernatant was passed through a phenylboronate affinity column (Affi-Gel boronate, Bio-Rad) that captures cis-diols. After loading the supernatant, the column was washed extensively with 10 column volumes of 0.1 M phosphate buffer (pH 7.4), 10 volumes of 2.5 mM ammonium bicarbonate, and 10 volumes of MilliQ water. Bound ligands were then eluted with 10 volumes of 5% acetic acid and lyophilized. The isolated sample was redissolved in 1% acetic acid for UPLC-MS/MS (Waters Xevo G2-XS) and 0.01 N for amino acid analysis (Hitachi High-Technologies L-8900).

In-situ SAXS during tensile testing

Eggcases were punched into dogbone shaped samples with a gauge length of 5 mm, and a width of 2 mm. DTT-treated samples were treated with 10 mM DTT in artificial seawater (450 mM NaCl, 10 mM KCl, 9 mM $CaCl_2$, 30 mM $MgCl_2$, and 16 mM $MgSO_4$) for at least 24 hours at 4˚C. Samples were then marked with a pair of permanent marker lines for optical strain tracking.

Three samples of each condition, native and DTT-treated, were uniaxially and symmetrically strained on a Linkam TST350 tensile stage at a rate of 50 µm s^{-1} during in-situ SAXS measurements at Beamline 7.3.3 of the Advanced Light Source[51]. The force, displacements of the markers (CCD camera), and x-ray scattering were recorded synchronously during in-situ SAXS during mechanical testing. X-ray scattering was collected on Dectris Pilatus3 2M detector, while samples were exposed to 10 keV x-rays for 0.5 s at 2.5 s intervals. Calibration of beam center and sample-to-detector distance with silver behenate and all SAXS data reduction were done using the Nika Package[52] on Igor Pro 8.

Macroscopic strains were measured by determining the change in centroid-to-centroid distance of the lines (Δl) with respect to the initial distance(l_0), using the equation $\varepsilon = \Delta l/l_0$. Nanoribbon strains and corresponding diffraction intensity for Fig. 3.3b were obtained by line integrations parallel to the stress axis, followed by fitting the curve with a Voigt function and an exponential baseline subtraction. Strains were calculated by converting q-space to d-space and applying the equation $\varepsilon_r = \Delta d/d_0$ where Δd is the change in d-spacings and d_0 the d-spacing of the unstrained material. Comparison of peak intensity was done with the height of the fitted curves.

Approximation of nanoribbon strain distribution for Fig. 3.3d were processed by masking q* peak for each image in the egg case tensile data set, and successive fitting of the radial intensity of the 2q* peaks. Fitting was done from 0 to 180˚, in 1˚ increments, with the axis of tension defined at 0˚. The resulting set of q values were converted to d-spacings using $2\pi/q$. All images in the data set were similarly processed to yield complete measurements of the evolution of the d-spacings of the collagen fibrils, at every angle from 0 to 180˚, at every time point in the experiment. Nanoribbon strains were then calculated as before.

Polarized Optical Microscopy

Eggcase was cryosectioned with a cryostat (Leica CM1850) and sections were washed with MilliQ water to remove residual OCT compound. Cross-sections of the eggcase were then examined under an optical microscope (Olympus BX51) with cross polarizers (BX-POL) and imaged using a colored camera (Olympus DP73).

Atomic Force Microscopy and Force Spectroscopy

Cryo-sectioned samples were mounted under the AFM and investigated on a MFP-3D atomic force microscope (Asylum Research, Santa Barbara, USA) mounted on an inverted light microscope. AppNano FORTA silicon tips were used for all experiments, and their exact spring constant values (which usually ranged between 2 and 3.6 nN/nm) were experimentally assessed prior to every usage by the thermal tune method. Deflection sensitivity was determined using glass as an indefinitely stiff reference material All images were recorded in AC mode at scan rates of 0.7 Hz.

Force spectroscopy measurements were performed with a loading force of 50 nN and loading/unloading rate of 250 nm/s. was chosen with respect to Buckle's one-tenth law[53] to mitigate any influence of the underlying layers. Force maps with resolutions of 24 × 24 pixels (576 force curves) were then recorded over the previously imaged areas, and stiffness values were extracted with the Asylum Research MFP-3D Hertz analysis tool by using the upper 60% of the approach curve, a half-angle of 20°, and a Poisson ratio of 0.33 to fit the model. The calculated stiffness values were then spatially plotted to yield a color-coded stiffness map with OriginLabs 8.5. A two-dimensional spline interpolation was performed on these maps to smoothen the visual presentation of the data. Peak values in the binned stiffness distributions were identified via the Origin Peak Analysis feature.

3.6 APPENDIX B

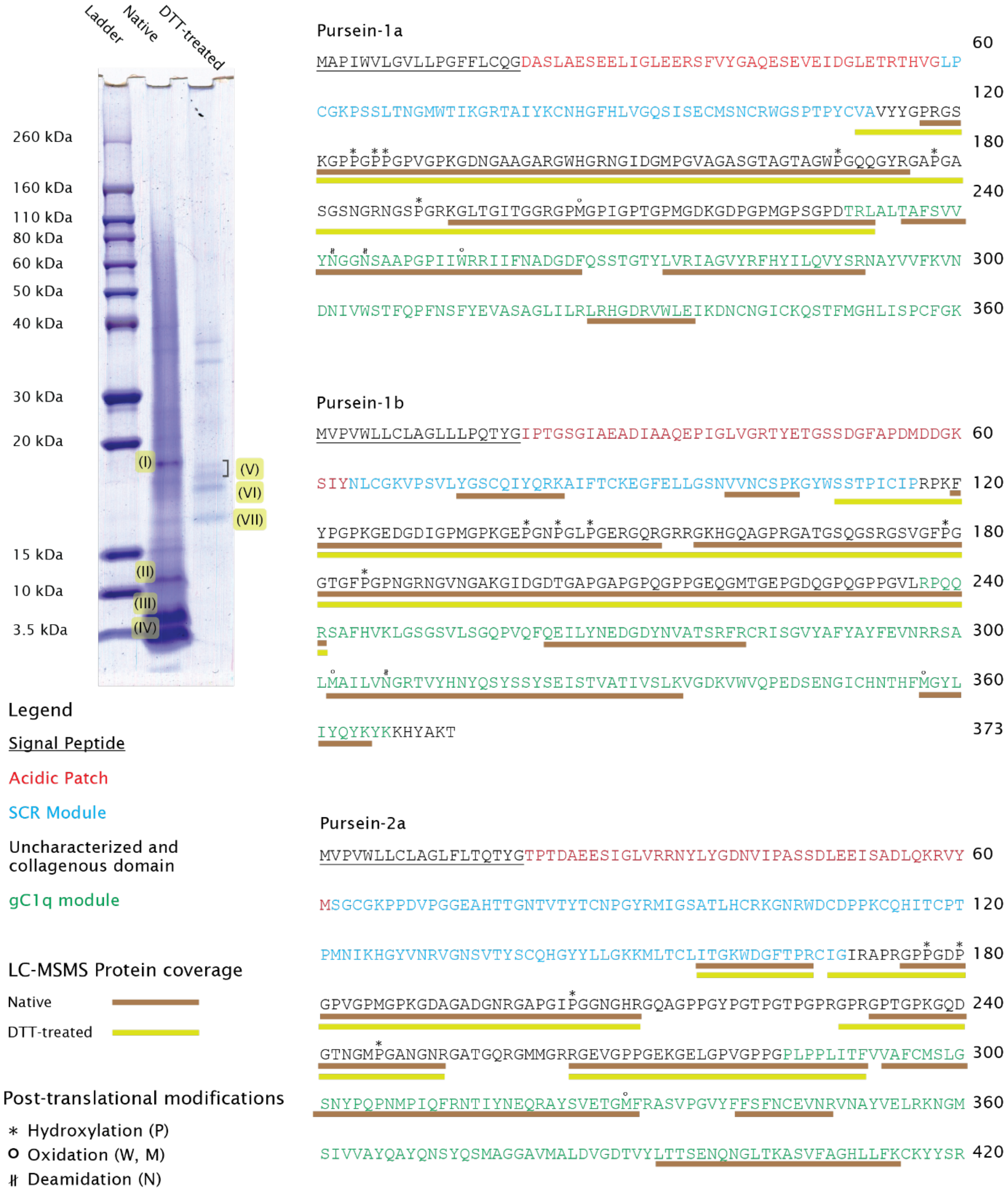

Fig. B1. SDS-PAGE of pepsinized native and DTT-treated eggcase. Bands (V), (VI) and (VIII) are fragments of collagenous domains, (III) and (IV) of NC1 and NC2, and (I) and (II) are a mixture of collagenous and NC domains. Corresponding protein sequence coverage and variable PTMs are indicated on the sequence.

(a)

```
Human_gC1qA             ----KDQPRPAFSAIR--RNPPMGGNVVIFDTVITNQEEPYQNHSGRFVCTVPGYYYFTF   163
Human_gC1qB             ----KATQKIAFSATRTINVPLRRDQTIRFDHVITNMNNNYEPRSGKFTCKVPGLYYFTY   172
Human_gC1qC             ----KQKFQSVFTVTRQTHQPPAPNSLIRFNAVLTNPQGDYDTSTGKFTCKVPGLYYFVY   170
Human_Col10A1_gC1q      ----TGMPVSAFTVILSKAYP-AIGTPIPFDKILYNRQQHYDPRTGIFTCQIPGIYYFSY   601
Human_Col8A1_gC1q       ----PAYEMPAFTAELTAPFP-PVGAPVKFNKLLYNGRQNYNPQTGIFTCEVPGVYYFAY   665
Human_Col8A2_gC1q       ----SAHATPAFTAVLTSPFP-ASGMPVKFDRTLYNGHSGYNPATGIFTCPVGGVYYFAY   624
Pursein-2a_gC1q         PLPPLITFVVAFCMSLGSNYP-QPNMPIQFRNTIYNEQRAYSVETGMFRASVPGVYFFSF   342
Pursein-1a_gC           ----TRLALTAFSVVYNGGNS-AAPGPIIWRRIIFNADGDFQSSTGTYLVRIAGVYRFHY   284
Pursein-1b_gC1          ----RPQQRSAFHVKLGSGSV-LSGQPVQFQEILYNEDGDYNVATSRFRCRISGVYAFYA   291
                                  .*               : :   : *    :.  :. :   : * * *

Human_gC1qA             QVLSQW-EICLSIVSSSRGQVRRSLGFCDTTNKGLFQVVSGGMVLQLQQGDQVWVEKD-P   221
Human_gC1qB             HASSRG-NLCVNLMRGR-ERAQKVVTFCDYAYN-TFQVTTGGMVLKLEQGENVFLQAT-D   228
Human_gC1qC             HASHTA-NLCVLLYRS----GVKVVTFCGHTSK-TNQVNSGGVLLRLQVGEEVWLAVN-D   223
Human_Col10A1_gC1q      HVHVKGTHVWVGLYKN----GTPVMYTYDEYTKGYLDQASGSAIIDLTENDQVWLQLPNA   657
Human_Col8A1_gC1q       HVHCKGGNVWVALFKN----NEPVMYTYDEYKKGFLDQASGSAVLLLRPGDRVFLQMPSE   721
Human_Col8A2_gC1q       HVHVKGTNVWVALYKN----NVPATYTYDEYKKGYLDQASGGAVLQLRPNDQVWVQMPSD   680
Pursein-2a_gC1q         NCEVNRVNAYVELRKN----GMSIVVAYQAYQN-SYQSMAGGAVMALDVGDTVYLTTS-E   396
Pursein-1a_gC1q         ILQVYSRNAYVVFKVN----DNIVWSTFQPFNS-FYEVASAGLILRLRHGDRVWLEIK-D   338
Pursein-1b_gC1q         YFEVNRRSALMAILVN----GRTVYHNYQSYSS-YSEISTVATIVSLKVGDKVWVQPE-D   345
                                  : :  .                .   :  : . :: *  .: *::

Human_gC1qA             KKGHIYQGSEADSVFSGFLIFPSA---- 245
Human_gC1qB             KNS-LLGMEGANSIFSGFLLFPDMEA-- 253
Human_gC1qC             YYD-MVGIQGSDSVFSGFLLFPD----- 245
Human_Col10A1_gC1q      ESNGLYSSEYVHSSFSGFLVAPM----- 680
Human_Col8A1_gC1q       QAAGLYAGQYVHSSFSGYLLYPM----- 744
Human_Col8A2_gC1q       QANGLYSTEYIHSSFSGFLLCPT----- 703
Pursein-2a_gC1q         NQNGLT----KASVFAGHLLFKCKYYSR 420
Pursein-1a_gC1q         NCNGIC----KQSTFMGHLISPCFGK-- 360
Pursein-1b_gC1q         SENGIC----HNTHFMGYLIYQYKYK-- 367
                            :       : * *.*:
```

(b)

```
HumanCR1_SCR24      ISCEPPPTISNGDFYSNNRTSFHNGTVVTYQCHTGPDGEQLFELVGERSIYCTSKDDQVG       1576
HumanCR1_SCR25      NKCTAPEVEN-AIRVPGNRSFFSLTEIIRFRCQPG------FVMVGSHTVQCQT----NG       1637
Pursein-2a_SCR1     SGCGKPPD------VP-GGEAHTTGNTVTYTCNPG------YRMIGSATLHCRK----GN       104
Pursein-2a_SCR2     ITCPTPMN------IK-HGYVNRVGNSVTYSCQHG------YYLLGKKMLTCLI----TG       158
Pursein-1a_SCR      LPCGKPSS------LT-NGMWTIKGRTAIYKCNHG------FHLVGQSISECMS----NC       101
Pursein-1b_SCR      NLCGKVPS------VL-YGSCQIYQRKAIFTCKEG------FELLGSNVVNCSP----KG       106
                      *                          : *: *      : ::*.     *

HumanCR1_SCR24      VWSSPPPRCIS  1587
HumanCR1_SCR25      RWGPKLPHC--  1646
Pursein-2a_SCR1     RWDCDPPKCQH  115
Pursein-2a_SCR2     KWDGFTPRCIG  169
Pursein-1a_SCR      RWGSPTPYCVA  112
Pursein-1b_SCR      YWSS-TPICIP  116
                     *.   * *
```

* Conservation of a single residue

: Conservation between groups of strongly similar properties

. Conservation between groups of weakly similar properties

Fig. B2. Multiple sequence alignment of (a) gC1q and (b) SCR domains. Consensus sequences are in green.

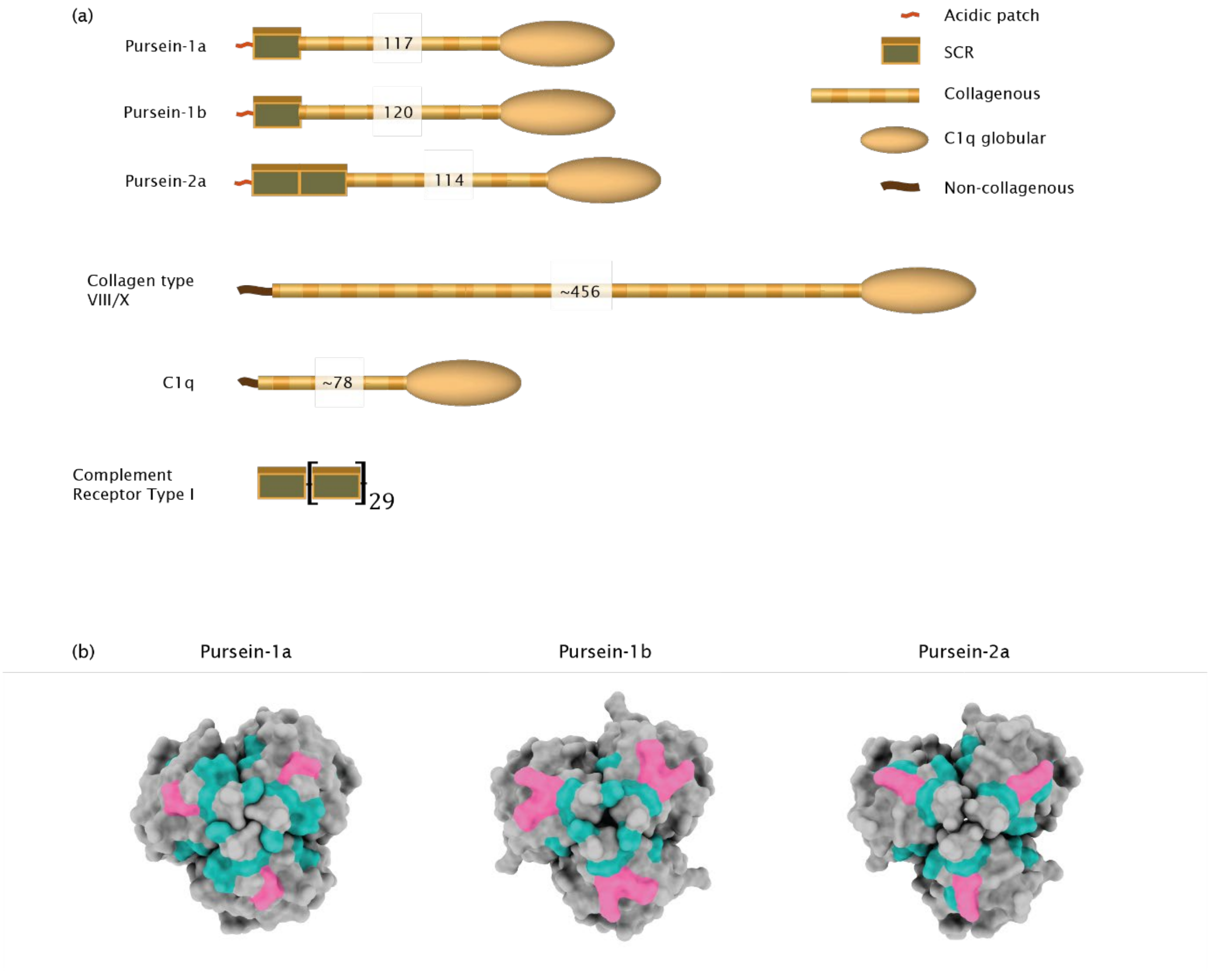

Fig. B3. (a) Illustration of domains in relevant proteins. (b) Surface illustration of aromatic residues seen in homology models of Purseins. Crystal structure of homotrimeric gC1q (NC1) of collagen type X was used as template. Aromatic residues are colored green and Arg residues in the vicinity of the aromatic 'crown' are colored pink.

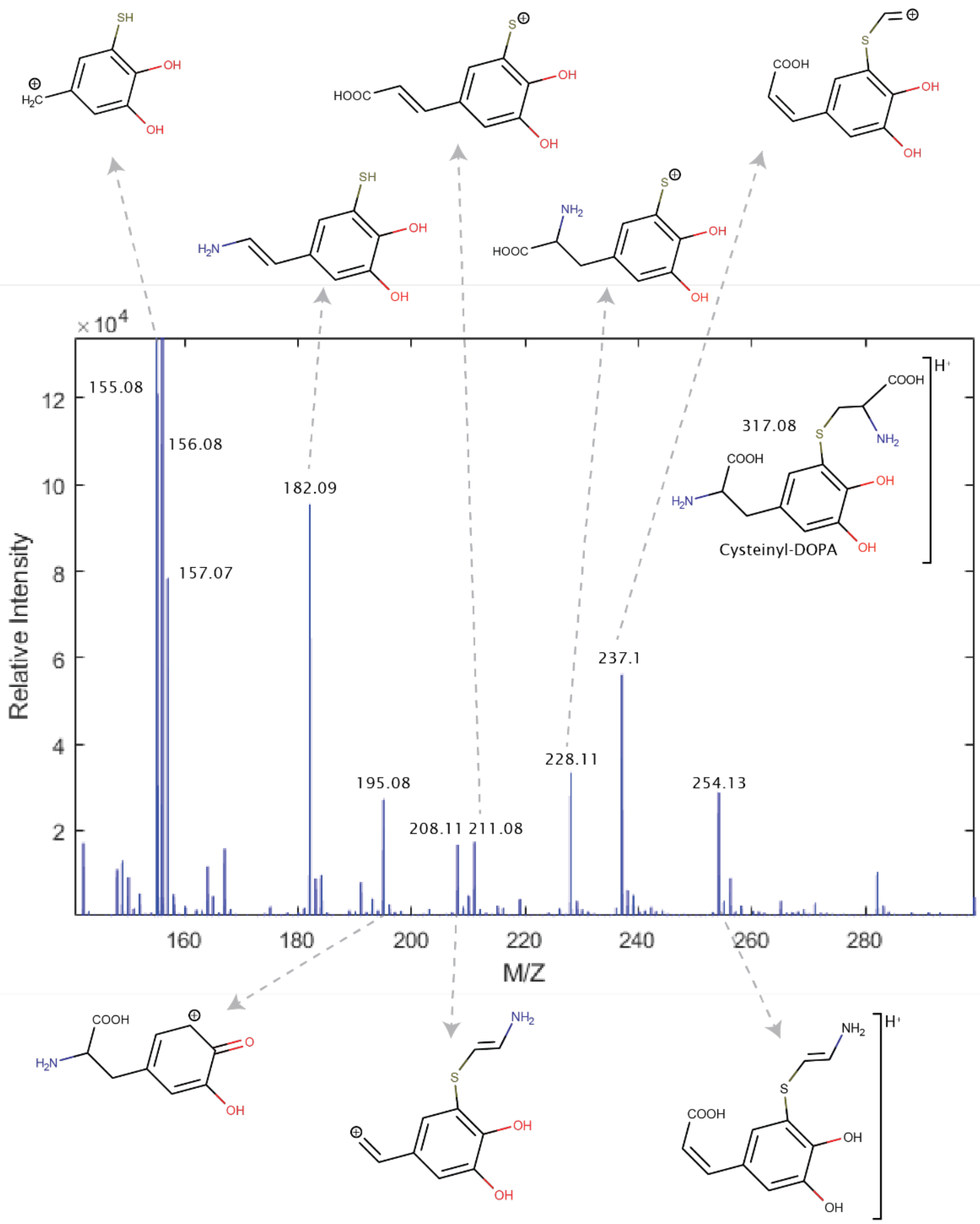

Fig. B4. LC-MS/MS of cysteinyl-DOPA (parent mass 317.08 Da).

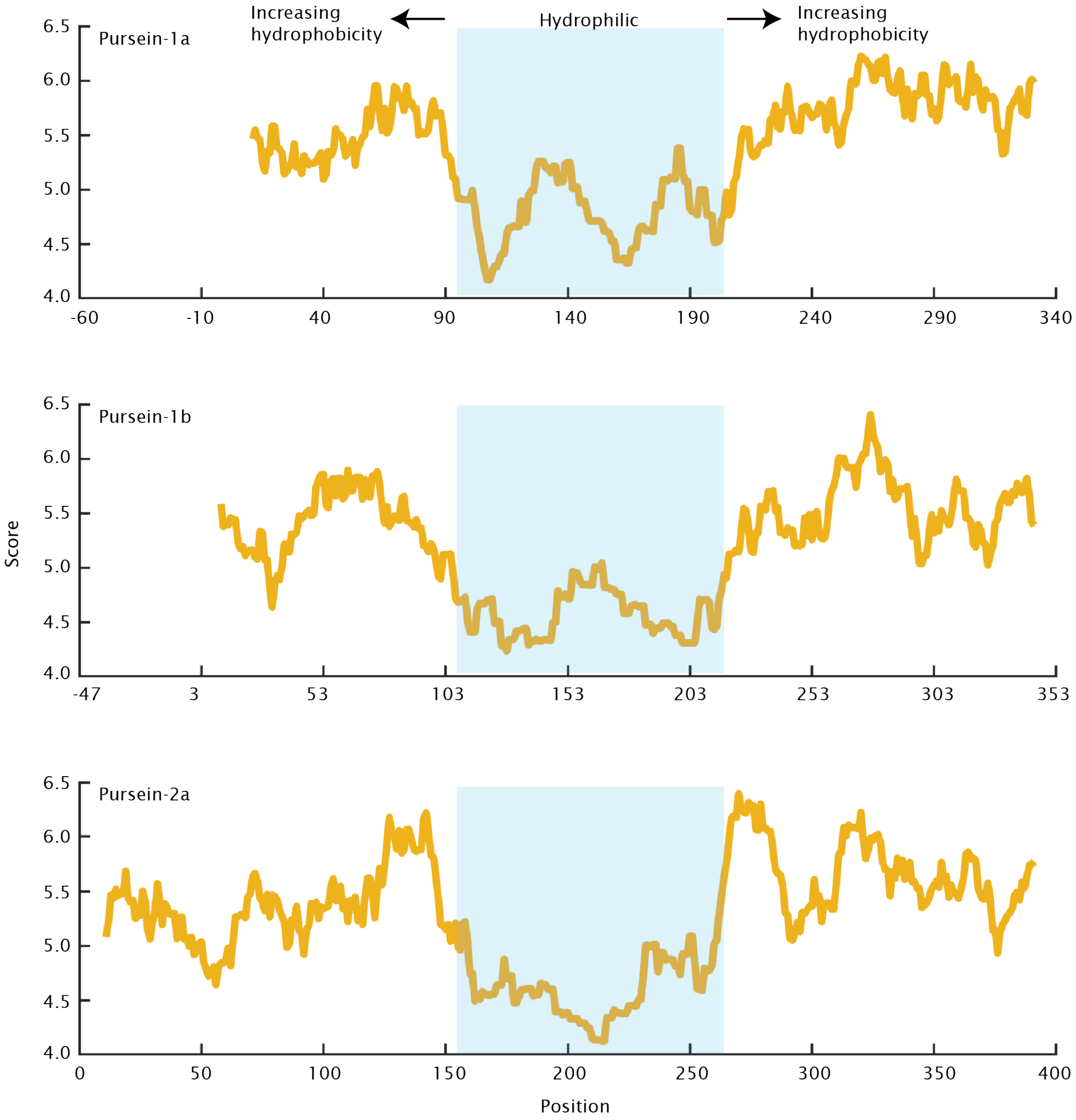

Fig. B5. Hydropathy plot of purseins with sequences aligned by their C-termini.

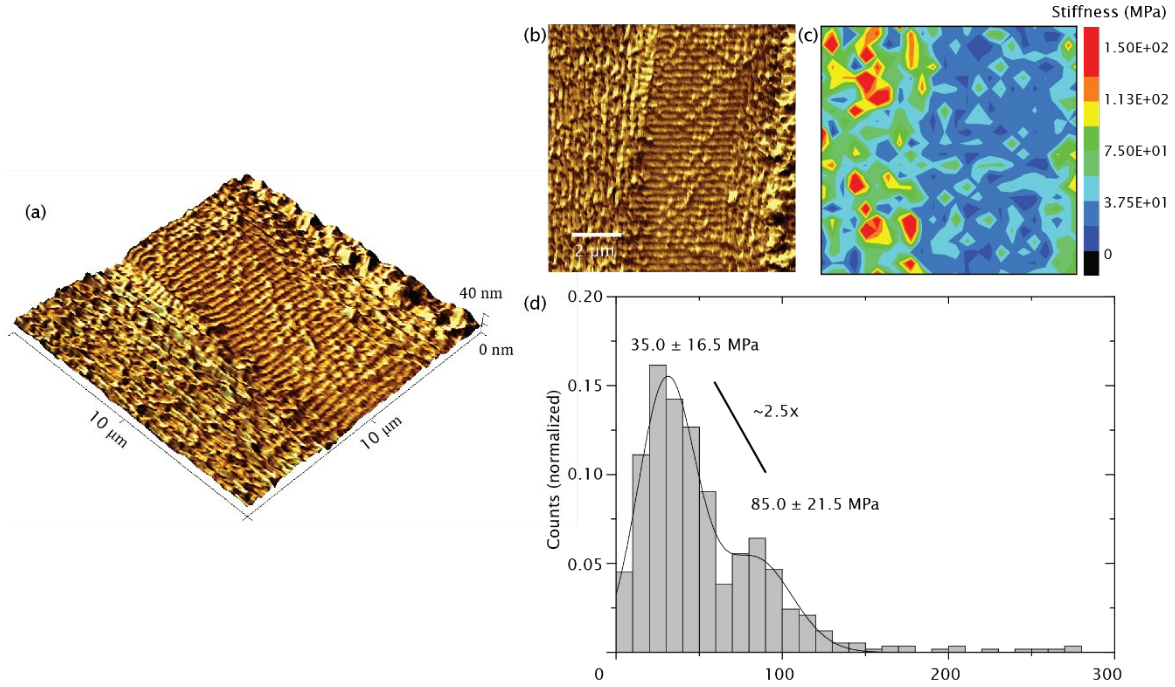

Fig. B6. (a) Atomic force microscopy of cross-section of the eggcase. (b) Phase image corresponding to two rows of nanoribbons aligned at different orientation with respect to the probe. (c) Force map emphasizing the orientation-dependent mechanical anisotropy. (d) Histogram indicating ~2.5x difference in modulus seen in force map.

	Pursein-1a	Pursein-1b	Pursein-2a	Average	Hydrolyzed egg case (Native)	Hydrolyzed egg case (Reduced)
Ala	6.74%	5.37%	5.74%	5.95%	4.58%	4.56%
Arg	5.87%	5.08%	5.99%	5.64%	4.41%	4.38%
Asn	4.69%	3.95%	5.99%	8.53%	11.86%	11.48%
Asp	3.52%	3.95%	3.49%			
Cys	2.35%	1.98%	2.99%	2.44%	0.23%	1.06%
Gln	2.35%	5.08%	3.24%	7.32	7.18%	7.11%
Glu	3.52%	4.52%	3.24%			
Gly	17.60%	16.95%	15.96%	16.83%	17.09%	16.79%
His	2.05%	1.69%	1.75%	1.83%	3.93%	3.87%
Ile	5.57%	5.08%	3.49%	4.72%	3.37%	3.35%
Leu	4.99%	3.95%	4.74%	4.56%	3.48%	3.41%
Lys	3.23%	4.80%	3.74%	3.92%	4.11%	4.14%
Met	2.05%	1.41%	3.49%	2.32%	2.09%	2.10%
Phe	3.52%	3.39%	2.49%	3.13%	2.71%	2.76%
Pro	7.92%	8.76%	10.47%	9.05%	8.68%	8.73%
Hyp					1.88%	1.92%
Ser	7.62%	7.63%	4.74%	6.66%	5.17%	5.05%
Thr	4.99%	4.24%	6.48%	5.24%	5.00%	4.90%
Trp	2.05%	0.56%	0.50%	1.04%		
Tyr	3.81%	5.65%	5.24%	4.90%	8.42%	8.48%
Val	5.57%	5.93%	6.23%	5.91%	5.40%	5.49%
DOPA					0.42%	0.42%

Table B1. Amino acid composition of virtual sequences (without signal peptides) and eggcase hydrolysates.

Name	*m/z*	Chemical structure
Cys-DOPA	317.09	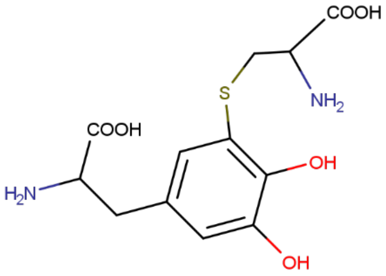
His-DOPA	351.19	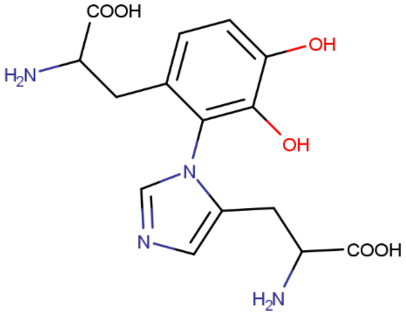

Table B2. Crosslinks observed during LC-MS with their corresponding m/z and chemical structure.

3.7 ACKNOWLEDGMENTS

This work was done in collaboration with E. Yoshida, Eric Schaible, R. Behrens, C. Monnier, B. Killingsworth, K.W. Kong, S.H. Hiew, A. Miserez, S. Hoon, and J. Herbert Waite.

We thank R. Segalman, Scott P.O. Danielsen, and K.S. Qwah for the productive discussions, C. Pierre, C. Orsini and S. Simon from UCSB Marine Operations and The REEF for the collection and generous contribution of the eggcases. We would also like to acknowledge the contribution of D. Morton for facilitating the donation of the nidamental gland after the parasitology class. Lastly, we thank L.L. Tan, and D. Ignatenko for their technical assistance. The research reported here was supported in part by the National Science Foundation (NSF) Materials Research Science and Engineering Center (MRSEC) at UC Santa Barbara (NSF DMR 1720256) through IRG-3. Individual fellowship support of R.G. was provided by Agency for Science, Technology and Research (A*STAR). X-ray scattering was performed at the Advanced Light Source, a DOE Office of Science User Facility (DE-AC02-05CH11231; beamline 7.3.3). We acknowledge the use of the shared facilities of the NSF MRSEC (DMR 1720256), the NRI-MCDB Microscopy Facility, and the research facilities within California NanoSystems Institute, supported by UC Santa Barbara, and the UC Office of the President at UC, Santa Barbara.

3.8 REFERENCES

1. Madison, K. C. Barrier Function of the Skin: “La Raison d’Être” of the Epidermis. *J. Invest. Dermatol.* **121**, 231–241 (2003).
2. Tullett, S. G. & Deeming, D. C. The relationship between eggshell porosity and oxygen consumption of the embryo in the domestic fowl. *Comp. Biochem. Physiol. A Physiol.* **72**, 529–533 (1982).
3. Goh, R., Danielsen, S., Schaible, E., McMeeking, R. & Waite, J. H. Nanolatticed architecture mitigates damage in shark eggcases. In *prep* (2021).
4. Knight, D. P., Feng, D. & Stewart, M. Structure and Function of the Salachian Egg Case. *Biol. Rev.* **71**, 81–111 (1996).
5. Knight, D. P., Feng, D., Stewart, M. & King, E. Changes in macromolecular organization in collagen assemblies during secretion in the nidamental gland and formation of the egg capsule wall in the dogfish Scyliorhinus canicula. *Philos. Trans. R. Soc. Lond. B. Biol. Sci.* **341**, 419–436 (1993).
6. Feng, D. & Knight, D. P. The effect of pH on fibrillogenesis of collagen in the egg capsule of the dogfish, Scyliorhinus canicula. *Tissue Cell* **26**, 649–659 (1994).
7. Knight, D. P. & Vollrath, F. Biological liquid crystal elastomers. *Philos. Trans. R. Soc. Lond. B. Biol. Sci.* **357**, 155–163 (2002).
8. Guerette, P. A. *et al.* Accelerating the design of biomimetic materials by integrating RNA-seq with proteomics and materials science. *Nat. Biotechnol.* **31**, 908–915 (2013).
9. Kishore, U. *et al.* Structural and functional anatomy of the globular domain of complement protein C1q. *Immunol. Lett.* **95**, 113–128 (2004).
10. Kirkitadze, M. D. & Barlow, P. N. Structure and flexibility of the multiple domain proteins that regulate complement activation. *Immunol. Rev.* **180**, 146–161 (2001).
11. Ariga, K. *et al.* Self-assembly as a key player for materials nanoarchitectonics. *Sci. Technol. Adv. Mater.* **20**, 51–95 (2019).
12. Bauer, J. *et al.* Nanolattices: An Emerging Class of Mechanical Metamaterials. *Adv. Mater.* **29**, 1701850 (2017).
13. Barclay, G. G. & Ober, C. K. Liquid crystalline and rigid-rod networks. *Prog. Polym. Sci.* **18**, 899–945 (1993).
14. Landsman, M. R. *et al.* Water Treatment: Are Membranes the Panacea? *Annu. Rev. Chem. Biomol. Eng.* **11**, 559–585 (2020).
15. Lim, F. & Sun, A. M. Microencapsulated islets as bioartificial endocrine pancreas. *Science* **210**, 908–910 (1980).
16. Desai, T. A., Hansford, D. & Ferrari, M. Characterization of micromachined silicon membranes for immunoisolation and bioseparation applications. *J. Membr. Sci.* **159**, 221–231 (1999).
17. Luong, T.-T., Boutillon, M.-M., Garrone, R. & Knight, D. P. Characterization of Selachian Egg Case Collagen. *Biochem. Biophys. Res. Commun.* **250**, 657–663 (1998).
18. Grabherr, M. G. *et al.* Full-length transcriptome assembly from RNA-Seq data without a reference genome. *Nat. Biotechnol.* **29**, 644–652 (2011).

19. Qin, X. & Waite, J. H. Exotic collagen gradients in the byssus of the mussel Mytilus edulis. *J. Exp. Biol.* **198**, 633–644 (1995).
20. Sagert, J. & Waite, J. H. Hyperunstable matrix proteins in the byssus of Mytilus galloprovincialis. *J. Exp. Biol.* **212**, 2224–2236 (2009).
21. Robinson, A. B. & Rudd, C. J. Deamidation of Glutaminyl and Asparaginyl Residues in Peptides and Proteins. in *Current Topics in Cellular Regulation* (eds. Horecker, B. L. & Stadtman, E. R.) vol. 8 247–295 (Academic Press, 1974).
22. Persikov, A. V., Ramshaw, J. A. M., Kirkpatrick, A. & Brodsky, B. Amino Acid Propensities for the Collagen Triple-Helix. *Biochemistry* **39**, 14960–14967 (2000).
23. Kishore, U. *et al.* C1q and tumor necrosis factor superfamily: modularity and versatility. *Trends Immunol.* **25**, 551–561 (2004).
24. Altschul, S. F., Gish, W., Miller, W., Myers, E. W. & Lipman, D. J. Basic local alignment search tool. *J. Mol. Biol.* **215**, 403–410 (1990).
25. Joung, S.-J., Chen, C.-T., Clark, E., Uchida, S. & Huang, W. Y. P. The whale shark, Rhincodon typus, is a livebearer: 300 embryos found in one 'megamamma' supreme. *Environ. Biol. Fishes* **46**, 219–223 (1996).
26. Koch, E. A., Spitzer, R. H., Pithawalla, R. B. & Parry, D. A. An unusual intermediate filament subunit from the cytoskeletal biopolymer released extracellularly into seawater by the primitive hagfish (Eptatretus stouti). *J. Cell Sci.* **107**, 3133–3144 (1994).
27. Zhao, H. & Waite, J. H. Coating Proteins: Structure and Cross-Linking in fp-1 from the Green Shell Mussel Perna canaliculus,. *Biochemistry* **44**, 15915–15923 (2005).
28. Zhao, H., Sun, C., Stewart, R. J. & Waite, J. H. Cement Proteins of the Tube-building Polychaete Phragmatopoma californica*,. *J. Biol. Chem.* **280**, 42938–42944 (2005).
29. Jacquet, M. *et al.* C1q and Mannose-Binding Lectin Interact with CR1 in the Same Region on CCP24-25 Modules. *Front. Immunol.* **9**, (2018).
30. Klickstein, L. B., Barbashov, S. F., Liu, T., Jack, R. M. & Nicholson-Weller, A. Complement Receptor Type 1 (CR1, CD35) Is a Receptor for C1q. *Immunity* **7**, 345–355 (1997).
31. Zhang, Y. & Chen, Q. The Noncollagenous Domain 1 of Type X Collagen: A NOVEL MOTIF FOR TRIMER AND HIGHER ORDER MULTIMER FORMATION WITHOUT A TRIPLE HELIX *. *J. Biol. Chem.* **274**, 22409–22413 (1999).
32. Boudko, S. P., Engel, J. & Bächinger, H. P. The crucial role of trimerization domains in collagen folding. *Int. J. Biochem. Cell Biol.* **44**, 21–32 (2012).
33. Bogin, O. *et al.* Insight into Schmid Metaphyseal Chondrodysplasia from the Crystal Structure of the Collagen X NC1 Domain Trimer. *Structure* **10**, 165–173 (2002).
34. Kvansakul, M., Bogin, O., Hohenester, E. & Yayon, A. Crystal structure of the collagen α1(VIII) NC1 trimer. *Matrix Biol.* **22**, 145–152 (2003).
35. Gallivan, J. P. & Dougherty, D. A. Cation-π interactions in structural biology. *Proc. Natl. Acad. Sci.* **96**, 9459–9464 (1999).
36. Fischer, P. & Finkelmann, H. Lyotropic liquid-crystalline elastomers. in *Structure, Dynamics and Properties of Disperse Colloidal Systems* (eds. Rehage, H. & Peschel, G.) 127–134 (Steinkopff, 1998). doi:10.1007/BFb0118121.

37. Bhattacharjee, A. & Bansal, M. Collagen Structure: The Madras Triple Helix and the Current Scenario. *IUBMB Life* **57**, 161–172 (2005).
38. Harrington, M. J., Gupta, H. S., Fratzl, P. & Waite, J. H. Collagen insulated from tensile damage by domains that unfold reversibly: In situ X-ray investigation of mechanical yield and damage repair in the mussel byssus. *J. Struct. Biol.* **167**, 47–54 (2009).
39. Knupp, C., Chew, M. & Squire, J. Collagen Packing in the Dogfish Egg Case Wall. *J. Struct. Biol.* **122**, 101–110 (1998).
40. Aßfalg, N. & Finkelmann, H. A Smectic A Liquid Single Crystal Elastomer (LSCE): Phase Behavior and Mechanical Anisotropy. *Macromol. Chem. Phys.* **202**, 794–800 (2001).
41. Kirkness, M. W., Lehmann, K. & Forde, N. R. Mechanics and structural stability of the collagen triple helix. *Curr. Opin. Chem. Biol.* **53**, 98–105 (2019).
42. D. Rey, A. Liquid crystal models of biological materials and processes. *Soft Matter* **6**, 3402–3429 (2010).
43. Bonn, D., Meunier, J., Greffier, O., Al-Kahwaji, A. & Kellay, H. Bistability in non-Newtonian flow: Rheology of lyotropic liquid crystals. *Phys. Rev. E* **58**, 2115–2118 (1998).
44. Ye, J. *et al.* Primer-BLAST: A tool to design target-specific primers for polymerase chain reaction. *BMC Bioinformatics* **13**, 134 (2012).
45. Almagro Armenteros, J. J. *et al.* SignalP 5.0 improves signal peptide predictions using deep neural networks. *Nat. Biotechnol.* **37**, 420–423 (2019).
46. F, M. *et al.* The EMBL-EBI search and sequence analysis tools APIs in 2019. *Nucleic Acids Res.* **47**, W636–W641 (2019).
47. de Castro, E. *et al.* ScanProsite: detection of PROSITE signature matches and ProRule-associated functional and structural residues in proteins. *Nucleic Acids Res.* **34**, W362-365 (2006).
48. Waterhouse, A. *et al.* SWISS-MODEL: homology modelling of protein structures and complexes. *Nucleic Acids Res.* **46**, W296–W303 (2018).
49. Pettersen, E. F. *et al.* UCSF ChimeraX: Structure visualization for researchers, educators, and developers. *Protein Sci.* **30**, 70–82 (2021).
50. Miyazawa, S. & Jernigan, R. L. Estimation of effective interresidue contact energies from protein crystal structures: quasi-chemical approximation. *Macromolecules* **18**, 534–552 (1985).
51. Montanaro, J., Gruber, D. & Leisch, N. Improved ultrastructure of marine invertebrates using non-toxic buffers. *PeerJ* **4**, e1860 (2016).
52. Ilavsky, J. Nika: software for two-dimensional data reduction. *J. Appl. Crystallogr.* **45**, 324–328 (2012).
53. Westbrook, J. H. & Conrad, H. *The Science of Hardness Testing and its Research Applications, American Society for Metals*.

4 CONCLUSION AND OUTLOOK

4.1 CONCLUSION

The swell shark eggcase is a multiphase fiber-reinforced soft composite that comprises laminates of nanoribbons oriented in a Bouligand-like twist. These nanoribbons are composed of a liquid crystalline derived nanolattice architecture. The non-cylindrical geometry of the nanoribbon is well-adapted to interfacial force distribution by maximizing surface area, while the nanolattice geometry provides novel toughening mechanisms.

In this dissertation, we have identified a series of asymmetry and lattice-governed deformation mechanisms that toughens the swell shark eggcase;

1) *A three-regime stepwise deformation mechanism involving a cumulative engagement of asymmetric fibers of different orientations into the deformation process.* The distinct decrease in modulus from one regime to another suggests a progressive and stepwise failure of components, and therefore prevents the catastrophic failure of the eggcase. The step-by-step decrease in modulus coincides with the engagement of fibers of different orientations as well as the formation of shear bands in the 2nd regime, and the disruption of the superlattice symmetry in the 3rd regime.

2) *A lattice-governed deformation mechanism involving uniform nucleation and formation of shear bands.* The uniform nucleation and formation of shear bands prevent the formation of a single critical shear band that would lead to catastrophic failure. Nucleation of shear bands was observed to form along the weak planes of the nanolattice architecture, serving as evidence that the uniform formation of shear bands is rooted in the asymmetry of the lattice.

3) *A lattice-governed deformation mechanism involving lattice reorientation.* Reorientation of the weak planes of the lattices towards the stress axis during strain facilitates shear band formation and plasticity.

The combination of geometric softening, cumulative nanoribbon engagement, and lattice-governed toughening mechanisms gives rise to a stepwise degradation of stiffness, strain hardening, and a high strain to failure. The basis of this unique architecture lies in the biochemistry and primary structure of the constituting protein. Leveraging transcriptomic and proteomic techniques, we have identified the protein of the eggcase, and the crosslinks involved in stabilization of the eggcase;

4) *A novel family of proteins, purseins, comprising three contiguous and modular series of domains typically associated with proteins found in the immune system — short consensus repeat (SCR), collagenous, and gC1q domains.* Analyses and interpretation of the sequence suggest an anisotropic rigid mid-block flanked by hydrophobic telechelic end domains that facilitates liquid crystalline (LC) supramolecular assembly.

5) *Cysteinyl cross-links.* Cysteines localized to the flanking non-collagenous domains were anticipated to form disulfide bonds based on sequence homology with SCR and gC1q domains. Additionally, cysteinyl-DOPA crosslinks were also identified using LC-MS/MS. Utilizing *in-situ* SAXS during tensile testing and deductions from observations during pepsin digestion of native and DTT-treated samples, these reducible crosslinks are involved in the mechanical and structural stabilization of the non-collagenous flanking domains.

6) *A conserved self-assembly strategy across eggcases of cartilaginous fishes.* Structurally homologous proteins comprising the same contiguous domains were observed in the genomes other oviparous and ovoviviparous chondrichthyans.

4.2 FUTURE DIRECTIONS

The most remarkable aspect of the tough and permeable swell shark eggcase is its exceptional architecture, which at various length scales serves as a versatile model system for a multitude of possible applications. The design strategies of the eggcase can be distinguished into the nanoarchitecture and the molecular structure of the constituting proteins that together enable and facilitate the self-assembly of the nanoarchitecture.

The nanoarchitecture of the eggcase comprises nanoribbons arranged into single-layer laminates with a Bouligand-like rotation from layer-to-layer. At this length scale, the eggcase resembles a multifunctional, multiphase fiber-reinforced soft composite with nanoribbons optimized for stress distribution. These nanoribbons are made of nanolattices that are similar to the lattice structures seen in mechanical metamaterials. In this case, the multifunctionality arises from the porosity of the mechanical metamaterial, therefore, enabling high toughness and permeability.

On the other hand, the novel self-assembly strategy delineates a new paradigm for materials derived from lyotropic liquid crystals. These multiphase heterogeneities (e.g. well-defined pores) and organization determine the final properties of materials derived from lyotropic LC, such as LC elastomers and nanoparticles. With regard to developing selective membranes and encapsulants for drug delivery applications, these properties can be exploited for encapsulation, templating, diffusion, release, reactions, or confinement of molecules. Therefore, there is already an active push towards techniques and self-assembly strategies that would allow formation and manipulation of the aqueous channel of lyotropic LCs, specifically the lattice symmetry and the lattice parameters[1].

As for swell shark eggcase, the macromolecular nature of pursein assembly enables larger aqueous channels, whereas the specificity of the supramolecular protein assembly determines the unique tetragonal lattice architecture. Above all, the mechanically robust and slowly biodegradable protein structure is processed under biologically compatible conditions — making related engineered structures attractive for protein or cellular encapsulation for drug delivery and immunoisolation applications.

Despite the major advances presented in this dissertation that could serve as an inspiration for nanoscale designs for mechanical metamaterials or molecular designs of lyotropic liquid crystals, isolation of the eggcase proteins as well as identifying conditions leading to self-assembly would be fundamentally important next steps to better understand the formation of the nanolattice architecture. This would eventually play an indispensable role in realizing the potential application of macromolecular lyotropic LCs.

4.3 REFERENCES

1. Mezzenga, R. Physics of Self-Assembly of Lyotropic Liquid Crystals. in *Self-Assembled Supramolecular Architectures* 1–20 (John Wiley & Sons, Ltd, 2012). doi:10.1002/9781118336632.ch1.